

Vapor-Liquid-Solid Growth of Monolayer MoS₂ Nanoribbons

Shisheng Li^{1,2}, Yung-Chang Lin³, Wen Zhao⁴, Jing Wu⁵, Zhuo Wang^{1,2}, Zehua Hu^{1,2}, Youde Shen⁶, Dai-Ming Tang⁷, Junyong Wang^{1,2}, Qi Zhang², Hai Zhu⁸, Leiqiang Chu^{1,2}, Weijie Zhao^{1,2}, Chang Liu⁹, Zhipei Sun¹⁰, Takaaki Taniguchi⁷, Minoru Osada⁷, Wei Chen^{1,2,8}, Qing-Hua Xu⁸, Andrew Thye Shen Wee^{1,2}, Kazu Suenaga³ Feng Ding^{4,11} and Goki Eda^{1,2,8}

¹ Centre for Advanced 2D Materials, National University of Singapore, 117542, Singapore

² Department of Physics, National University of Singapore, 117542, Singapore

³ Nanotube Research Center, National Institute of Advanced Industrial Science and Technology, Tsukuba 305-8564, Japan

⁴ Center for Multidimensional Carbon Materials, Institute for Basic Science, Ulsan, 689-798, Republic of Korea

⁵ Institute of Materials Research and Engineering, Agency for Science, Technology, and Research, 138634, Singapore

⁶ Department of Electrical and Computer Engineering, National University of Singapore, 117583, Singapore

⁷ International Center for Materials Nanoarchitectonics, National Institute for Materials Science, Tsukuba 305-0044, Japan

⁸ Department of Chemistry, National University of Singapore, 117543, Singapore

⁹ Institute of Metal Research, Chinese Academy of Sciences, Shenyang, 110016, China

¹⁰ Department of Micro and Nanosciences, Aalto University, Espoo FI-02150, Finland

¹¹ School of Materials Science and Engineering, Ulsan National Institute of Science and Technology, Ulsan, 689-798, Republic of Korea

Correspondence and requests for materials should be addressed to G.E. (email: g.eda@nus.edu.sg), S.L. (email: shishengli1108@gmail.com)

Chemical vapor deposition (CVD) of two-dimensional (2D) materials such as monolayer MoS₂ typically involves conversion of vapor-phase precursors to a solid product in a process that may be described as a vapor-solid-solid (VSS) mode. Here, we report the first demonstration of vapor-liquid-solid (VLS) growth of monolayer MoS₂ yielding highly crystalline ribbon-shaped structures with a width of a few tens of nanometers to a few micrometers. The VLS growth mode is triggered by the reaction between molybdenum oxide and sodium chloride, which results in the formation of molten Na-Mo-O droplets. These droplets mediate the growth of MoS₂ ribbons in the “crawling mode” when saturated with sulfur on a crystalline substrate. Our growth yields straight and kinked ribbons with a locally well-defined orientation, reflecting regular horizontal motion of the liquid droplets during growth. Using atomic-resolution scanning transmission electron microscopy (STEM) and second harmonic generation (SHG) microscopy, we show that the ribbons are homoepitaxially on monolayer MoS₂ surface with predominantly 2H- or 3R-type stacking. These findings pave the way to novel devices with structures of mixed dimensionalities.

Recent advances in the chemical vapor deposition (CVD) of two-dimensional (2D) transition metal dichalcogenides (TMDs) on various substrate surfaces^{1,2} have opened up new prospects for the exploration of their fundamental physical properties³ and practical device implementation schemes⁴. However, the range of structures that can be controllably synthesized by the current methods in terms of morphology, spatial selectivity, crystal orientation, layer number, and chemical composition is still limited. Development of versatile growth methods is essential to enabling the realization of highly integrated electronic and photonic devices based on these materials.

While various CVD-based growth techniques for TMDs have been demonstrated to date^{1,2}, they generally involve similar microscopic mechanism where the gas/vapor phase precursors are converted to a solid-state product via surface adsorption, surface diffusion, and bond formation⁵. This growth mode, which may be referred to as vapor-solid-solid (VSS) type, is common in the CVD growth of not only 2D TMDs⁶⁻⁹ but also other ultrathin chalcogenides¹⁰ as well as graphene¹¹⁻¹³. Since the precursors are uniformly supplied to the nuclei in the 2D growth plane, this type of growth yields structures with a characteristic crystal shape determined primarily by the inherent free energy of the crystal edges and surface diffusion kinetics¹⁴.

An alternative growth mode known as the vapor-liquid-solid (VLS) growth is an attractive approach to introducing lateral control in 2D crystal growth and achieving direct bottom-up synthesis of integration-ready nanostructures. In VLS mode, one-dimensional (1D) nanostructures are produced by precipitation from supersaturated catalytic liquid droplets¹⁵⁻¹⁷. VLS growth has been observed for various van der Waals layered compounds including BN¹⁸, NiCl₂¹⁹, SnS₂²⁰ and Bi₂Se₃²¹, but the growth products are often randomly oriented multilayered nanotubes or nanoribbons, typically consisting of tens to hundreds of monolayers. Meanwhile, recent demonstrations of graphene²² and 2D oxide²³ growth on liquid metal surfaces, and monolayer MoSe₂ growth on molten glass²⁴ highlight the unique potential of liquid-mediated synthesis techniques. Suzuki et al.²⁵ succeeded in VLS-like growth of laterally oriented graphene nanoribbons from molten nickel. Their observation suggests that non-tubular, atomically thin structures can be synthesized in VLS mode and offers prospects

towards the controlled 1D growth of layered compound semiconductors such as TMDs in their monolayer limit.

In this article, we report in-plane VLS growth of monolayer MoS₂ ribbons with an average width of hundreds of nanometers on crystalline surfaces. We discover that alkali metal halide reacts with transition metal oxide precursors to form molten droplets that crawl on the substrate surface and mediate the highly anisotropic growth. We demonstrate that the VLS mode allows homoepitaxial growth of ribbons on a pre-grown monolayer MoS₂ support layer, yielding unique 1D-on-2D structures. We also show that the alignment of the ribbons is largely determined by the orientation of the underlying crystal, similar to the guided horizontal growth of nanotubes²⁶ and nanowires²⁷. Our results provide insight into the distinctly new growth mode of 2D MoS₂ and offer prospects for their nanoelectronic device implementations.

VLS growth of MoS₂ nano- and micro-ribbons on a NaCl crystal

We conducted salt-assisted CVD⁹ of monolayer MoS₂ on a freshly cleaved surface of a NaCl single crystal using powder MoO₃ and S as precursors (See Methods and Supplementary Fig. 1 for details). Figure 1a and b show optical and atomic force microscope (AFM) images of monolayer MoS₂ grown on the NaCl surface (see also Supplementary Fig. 2 for more images). In stark contrast with the typical triangular crystals, straight and kinked narrow ribbons with a width of a few tens of nanometers to a few micrometers, and a length ranging from a few to tens of micrometers are grown (see Supplementary Fig. 2i for width distribution). The step height of a majority of these ribbons is ~ 0.8 nm, which is consistent with the thickness of monolayer MoS₂²⁸ (Supplementary Fig. 3). The optical images show that most ribbons are terminated with a particle as indicated by the circles in Figure 1a-c. We note that the size of these particles consistently matches the width of the ribbons. These are characteristic features of nanostructures resulting from the “crawling mode”^{26,27,29} of VLS growth where liquid droplets crawl on the surface as the reaction product is precipitated laterally. These ribbons are locally aligned but exhibit occasional regular kinks, suggesting that the growth is guided either by the substrate or the crystal facets of MoS₂ (Figure 1 a and d, Supplementary Fig. 2).

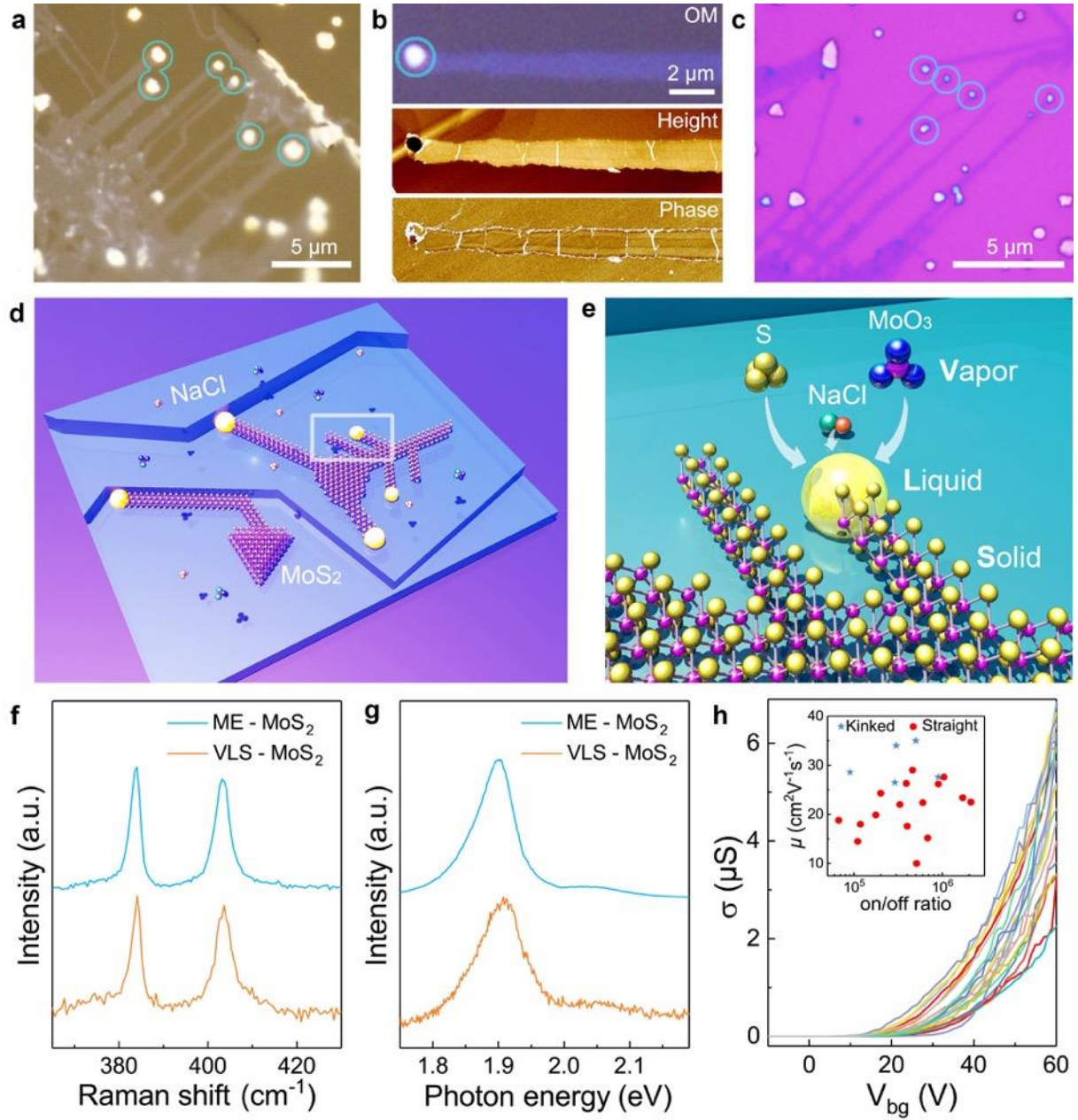


Figure 1 | Morphology and properties of VLS-MoS₂ ribbons grown on a NaCl single crystal. (a) Optical image of MoS₂ ribbons grown on a NaCl crystal. (b) Optical and corresponding AFM images of MoS₂ ribbons. (c) Optical image of MoS₂ ribbons transferred on a SiO₂/Si substrate. Circles highlight the terminal particles attached to the MoS₂ ribbons. (d, e) Schematic illustrations of VLS growth of MoS₂ ribbons on a NaCl crystal surface. The reaction involves: 1) formation of liquid phase Na-Mo-O in small droplets; 2) dissolution of sulfur in the droplet; 3) horizontal growth of MoS₂ ribbons and lateral displacement of the droplet. (f) Raman and (g) PL spectra of as-transferred MoS₂ ribbons and mechanically exfoliated (ME) monolayer MoS₂ on SiO₂/Si substrates. (h) Transport properties of MoS₂ nanoribbon FETs. Inset shows the plot of mobility versus current on/off ratio for all measured MoS₂ nanoribbon FETs.

To understand the possible reaction routes involving liquid-phase intermediate compound, we conducted thermogravimetric analysis (TGA) of the growth precursors, X-ray diffraction (XRD) and energy dispersive X-ray (EDX) analysis on the reaction products. While our growth temperature ($\sim 700\text{ }^{\circ}\text{C}$) is below the typical melting point of MoO_3 ($795\text{ }^{\circ}\text{C}$) and NaCl ($801\text{ }^{\circ}\text{C}$) in atmospheric pressure, these compounds gradually sublime at the growth temperature as evidenced by their deposition on SiO_2/Si substrate in a control experiment (Supplementary Fig. 4). TGA of $\text{MoO}_3\text{-NaCl}$ mixture (Supplementary Fig. 5) shows a prominent weight loss at $\sim 550\text{ }^{\circ}\text{C}$ in contrast to pure MoO_3 , which shows weight loss only above $800\text{ }^{\circ}\text{C}$. These results indicate that NaCl chemically reacts with MoO_3 at temperatures well below the melting point of the two compounds. Further, XRD study of the reaction product reveals that the resulting compound contains $\text{Na}_2\text{Mo}_2\text{O}_7$, which has a low melting point of $605\text{ }^{\circ}\text{C}$ ³⁰ and is a liquid at the growth temperature (Supplementary Figs. 4 and 5). A possible reaction route³¹ is



We experimentally found that the liquid phase $\text{Na}_2\text{Mo}_2\text{O}_7$ indeed yields MoS_2 when exposed to sulfur vapor at the growth temperature (Supplementary Fig. 5). From EDX analysis, the particles terminating the ribbons are found to contain molybdenum, sodium, oxygen, sulfur, and a small amount of chlorine (Supplementary Fig. 6). These results further support the validity of the above reaction route and VLS growth as schematically illustrated in Figures 1d and e.

Sodium plays a key role in lowering the melting point of MoO_3 precursor and enabling the VLS mode. This is similar to the role of gold in the VLS growth of Si and III-V semiconductor nanowires where gold forms a eutectic with the precursor element and facilitate liquid-mediated growth at temperatures lower than required in other growth modes^{15,17,27,29,32}. Alloys of alkali metal, transition metal and oxygen have similar melting points and can effectively mediate VLS growth of TMDs³³. We found that reacting pre-deposited sodium molybdate (Na_2MoO_4), which is also a liquid at $700\text{ }^{\circ}\text{C}$, with sulfur vapor yields monolayer MoS_2 ribbons, triangular crystals, and continuous thin films (Supplementary Figs. 7 and 8). This observation reveals a few important aspects of the

reaction. First, chlorine is not an essential element in triggering the VLS mode. Second, the growth can be achieved in absence of MoO_3 vapor. Third, the liquid phase precursor can also mediate 2D growth yielding a continuous film. Further, we tested the general applicability of this growth method by conducting the growth of other monolayer TMDs (MoSe_2 , WS_2 , WSe_2 , MoTe_2 , WTe_2) and their heterostructure ($\text{MoS}_2/\text{MoSe}_2$) by reacting Na_2MoO_4 and Na_2WO_4 with chalcogen vapors above their melting point (Supplementary Figs. 8 and 9). In all cases, the desired materials could be grown, indicating the versatility of this approach.

Raman spectrum of MoS_2 ribbons transferred on a SiO_2/Si substrate shows characteristic E_{2g}^1 and A_{1g} peaks at 384.2 and 403.7 cm^{-1} with a peak separation of 19.5 cm^{-1} (Figure 1f). The ribbons also exhibited characteristic excitonic photoluminescence (PL) peaks at 1.9 and 2.05 eV (Figure 1g). These features are nearly identical to those of mechanically exfoliated (ME-) monolayer MoS_2 , indicating that our VLS growth does not introduce substantial defects, strain and doping beyond the level of exfoliated materials. We further verified this by investigating the electronic quality of the nanoribbons by evaluating their field-effect mobility. We tested 21 two-terminal field-effect transistors (FET) based on straight and kinked MoS_2 nanoribbons and found that they exhibit typical n-type transfer characteristics with on/off ratio of $\sim 10^5$ and electron field-effect mobility range of 10-35 $\text{cm}^2\text{V}^{-1}\text{s}^{-1}$, which is comparable to the performance of monolayer MoS_2 prepared by mechanical exfoliation³⁴ and metal-organic CVD². Both types of ribbons exhibited similar average performance, indicating that kinks do not represent major structural defects detrimental to carrier transport at room temperature (Figure 1h).

VLS epitaxy of MoS_2 nano- and micro-ribbons on monolayer MoS_2

In order to test the feasibility of VLS growth on other surfaces, we further conducted salt-assisted growth of MoS_2 ribbons on a continuous film of monolayer MoS_2 pre-grown on a SiO_2/Si substrate (See Supplementary Information for detailed method). Figure 2a and Supplementary Fig. 10 show the unique morphology of kinked ribbons on monolayer MoS_2 support layer. Majority of these ribbons were found to be monolayers (Supplementary Fig. 11a-c). The orientation of the ribbons is locally well defined and their predominant growth directions are separated by $\sim 60^\circ$ or $\sim 120^\circ$ (Figure 2a). Most ribbons are terminated by a particle similar to the case of growth on NaCl single crystal (Figure 2a and b).

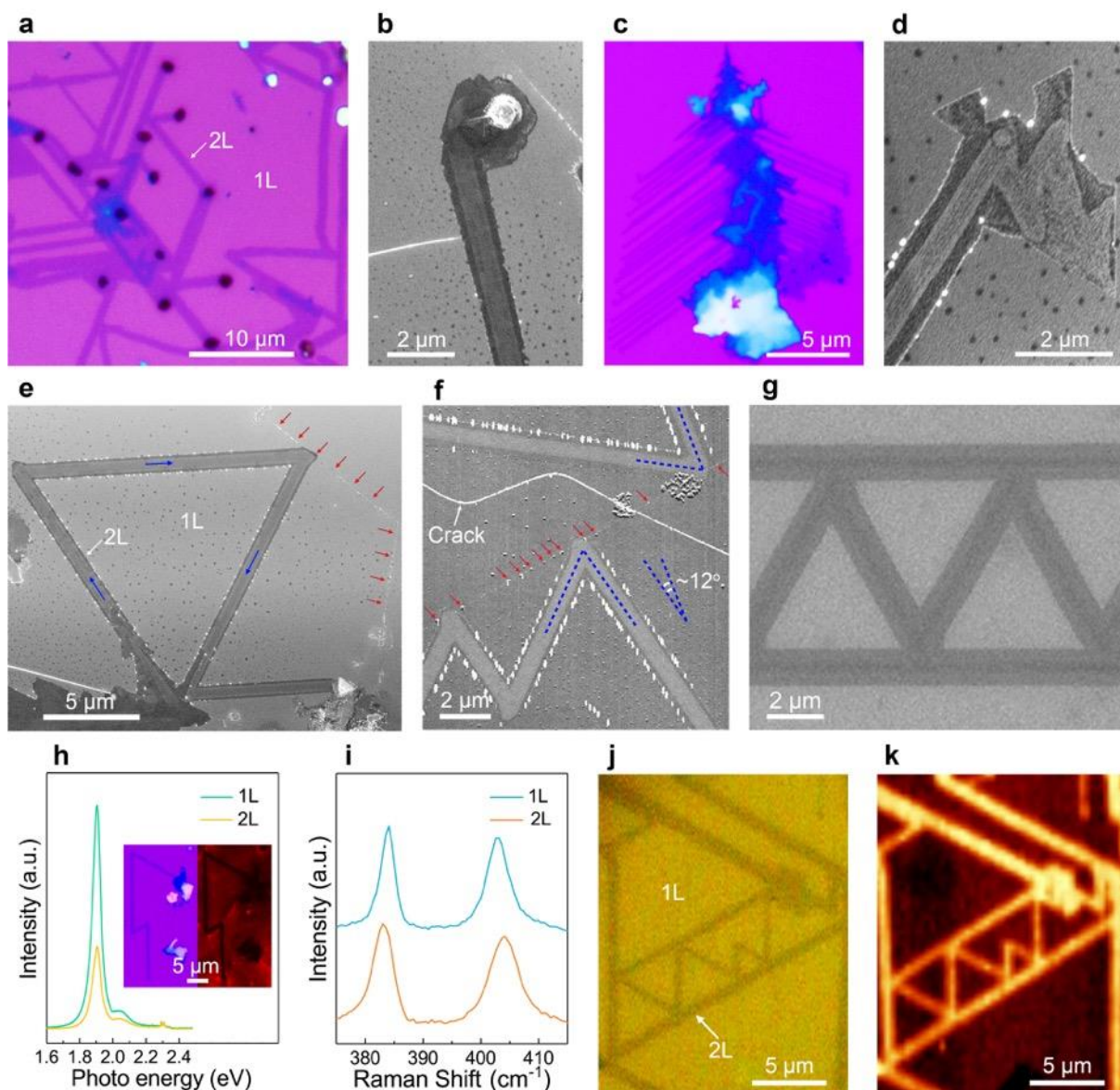


Figure 2 | VLS homoepitaxy of MoS₂ ribbons on monolayer MoS₂. (a) Optical image of ribbons on a monolayer MoS₂ film. (b) SEM image of a particle attached to the ribbon terminal. (c) Parallel arrays of ribbons extending from a MoS₂ crystal island. (d) SEM image of the terminal morphology of a ribbon in the array. (e) SEM and (f) AFM images of ribbons showing kinks at the line features (indicated by the arrows that point to the aggregated particles) of the underlying MoS₂. These line features are most likely the grain boundary of the underlying monolayer MoS₂ (See Supplementary Information for further discussions). (g) Zigzag-shaped MoS₂ ribbon which resulted from a liquid droplet trapped in between two parallel ribbons. (h) Micro-PL spectra collected from the underlying monolayer and an overgrown ribbon. Inset are optical and fluorescence images of the structure. (i) Raman spectra of underlying monolayer and an overgrown ribbon. (j) Optical image and (k) corresponding Raman A_{1g} intensity map of MoS₂ ribbons grown on monolayer MoS₂.

Figure 2c shows an optical image of arrays of numerous parallel nanoribbons extending from an island of multilayered MoS₂. This morphology suggests that the alignment of the ribbons is induced by the orientation of the underlying MoS₂ crystal. Figure 2d shows another frequently observed ribbon termination where a faceted 2D flake is formed instead of a particle. Absence of a particle suggests that the precursor was fully consumed during growth. Careful examination of the ribbon morphologies by scanning electron microscope (SEM) (Figure 2e) and AFM (Figure 2f) reveals that the kinks often appear along straight line features of the underlying monolayer MoS₂. Particles tend to aggregate along these lines as indicated by the arrows in Figure 2e and f. Based on a series of measurements, we found that these lines correspond to the grain boundary (GB) of the underlying MoS₂ (See Supplementary Fig. 11d-f for further discussions). The features of the ribbons around the kinks reveal the history of the liquid droplet migration. For example, the morphology of the ribbon in Figure 2e suggests that the droplet initially moved towards the upper left region before encountering a surface perturbation and changing its direction by $\sim 120^\circ$ as marked by the arrows. The growth of this ribbon was terminated after the droplet took two additional turns, one at a GB and another at a ribbon edge. It is also worth highlighting that each kink shows a round corner, which is indicative of the liquid state of the precursor at the growth temperature (Supplementary Figs. 6 and 11b). Figure 2f shows an AFM phase image of two ribbons grown on two adjacent grains of the underlying MoS₂ film. In both grains, the ribbon takes a $\sim 120^\circ$ turn at the GB but the orientations of the ribbons in the two adjacent grains are offset by $\sim 12^\circ$. The difference in the ribbon orientation is most likely caused by the orientation difference of the underlying MoS₂ grains. Another commonly observed scenario involves a droplet trapped in between two parallel MoS₂ ribbons as shown in Figure 2g. In this case, the liquid droplet “bounces” back and forth with $\sim 120^\circ$ turns between the parallel ribbons, resulting in a peculiar zigzag-shaped ribbon.

Micro-PL spectroscopy and fluorescence imaging show that the characteristic excitonic direct gap emission of monolayer MoS₂ is significantly quenched along the ribbons (Figure 2h). Quenching of PL suggests that there is a strong interaction between the upper and lower MoS₂ layers, resulting in indirect band gap formation in the bilayer regions^{35,36}. Raman spectra show that the E_{2g}¹ and A_{1g} peaks of the bilayer regions exhibit characteristic softening and stiffening as observed in commensurately stacked bilayers, further indicating strong interlayer

interaction (Figure 2i). Figure 2j and k are optical image and corresponding integrated intensity map of Raman A_{1g} peak of the nanoribbons, respectively, showing distinctly stronger and uniform intensity in the bilayer region, highlighting the structural uniformity of the epitaxial layer.

Stacking order of 1D-on-2D MoS₂ structures

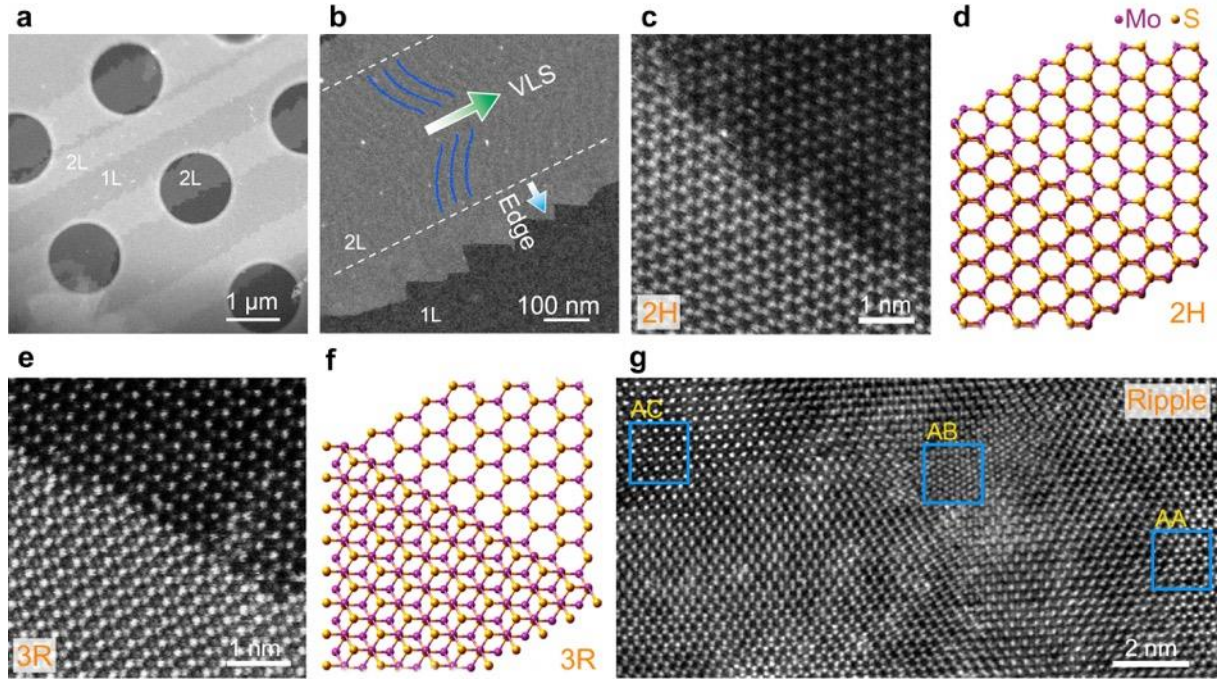


Figure 3 | STEM images of homoepitaxially grown MoS₂ ribbons on monolayer MoS₂. (a) ADF-STEM image of four parallel MoS₂ ribbons. The ribbons appear in bright contrast. (b) High-magnification TEM image showing the zigzag-shaped edges and fishbone-like contrast at the center of the ribbon. The arrows indicate edge regions where the contrast is uniform. (c) STEM image and (d) corresponding atomic configuration of the edge of a ribbon showing the boundary between 2H-stacked bilayer and supporting monolayer. (e) STEM image and (f) corresponding atomic configuration of an edge of a ribbon showing the boundary between 3R-type bilayer and supporting monolayer. Purple balls in (d) and (f) represent Mo atoms, and yellow balls represent S atoms. (g) STEM image showing spatially varying stacking sequence in the center region of a ribbon. AA, AB, and AC represent three different local stacking sequences.

To further investigate the stacking order of the epitaxially grown ribbons on monolayer MoS₂, we conducted scanning transmission electron microscopy (STEM) imaging of the samples. Figure 3a and b show a low-magnification annular dark field (ADF) STEM image of ribbons

on a monolayer MoS₂ support, revealing their rough zigzag-shaped edges. Atomic resolution STEM images near the edges of the bilayer regions reveals that two types of stacking orders, namely 2H and 3R, are predominant. Figure 3c and 3d show STEM image and corresponding atomic model of bilayer 2H-MoS₂. 2H-type bilayer is characterized by a stacking sequence where the two layers have 180 ° relative orientation, restoring inversion symmetry. The metal (chalcogen) atoms in the upper layer are aligned with the chalcogen (metal) atoms in the lower layer, thereby forming a hollow hexagonal structure when viewed from the c-axis direction (Figure 3d). Figure 3e and 3f show STEM image and corresponding atomic model of the 3R-type bilayer. This 3R stacking is characterized by a stacking sequence where the two layers have the same orientation but the top layer is shifted by $1/\sqrt{3}$ lattice constant along the $\langle 110 \rangle$ direction. These structures can be readily identified from the ADF contrast. The observed predominance of commensurate stacking is a direct evidence of epitaxial growth.

Detailed analysis of the atomic structure across the width of the ribbons reveals that the stacking order is spatially varied. Unlike the edge regions, which are uniform in contrast (blue arrow in Figure 3b), the center region of the ribbons exhibits peculiar fishbone-like periodic fringes (highlighted by blue lines in Figure 3b). These fringes suggest undulations of the layers with local strain and spatially varying interlayer interactions³⁷. Figure 3g shows the atomic-resolution STEM image of the center of the ribbon where the dominant stacking is of 2H-type. It can be seen that the stacking order changes across the ribbon from AC (left square), AB (middle square) to AA (right square) over several nanometers. Careful examination of the signal intensity reveals that the relative orientation of the two layers remains the same while the layers are locally displaced with respect to one another (Supplementary Fig. 12). Such an evolution is indicative of the presence of strain and local separation of the layers³⁷. As discussed below, the ripples may be induced a compressive force exerted by the liquid droplet during growth. It is worth noting that we did not find any evidence of Na and Cl impurities in the crystal lattice of MoS₂ based on the atomically resolved Z-contrast imaging of our samples.

Probing stacking order by non-linear optics

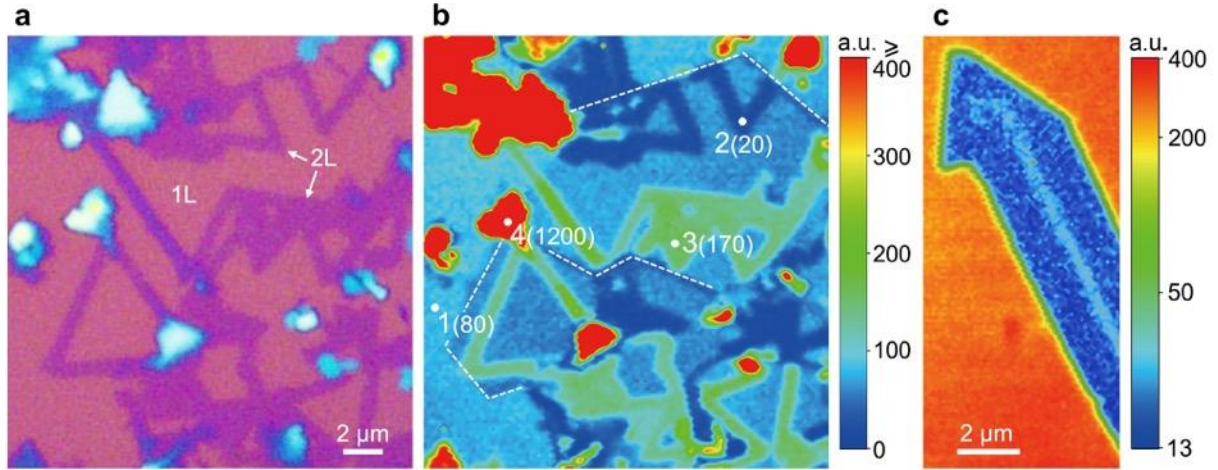


Figure 4 | SHG microscopy of homoepitaxially grown MoS₂ ribbons on monolayer MoS₂. (a) Optical image and (b) corresponding SHG image of MoS₂ ribbons and thick layers grown on monolayer MoS₂. The dark blue regions (point 2) in (b) represent ribbons exhibiting SHG signals weaker than the underlying monolayer (point 1). On the other hand, green regions (point 3) correspond to ribbons with SHG signals stronger than the underlying monolayer. The GBs of the underlying MoS₂ layer are identified from the contrast of SHG signal and highlighted with a dashed line. (c) SHG image of a ribbon with non-uniform SHG signal. The overall signal is weaker than the background suggesting that it is a bilayer with predominantly 2H phase. The signal is slightly enhanced in the center region of the ribbon due to the spatially varying of stacking sequence and weaker interlayer interaction.

Stacking order has a significant impact on the non-linear optical properties of MoS₂³⁸⁻⁴¹. In order to further investigate the spatial variations of stacking sequence in the homoepitaxially grown ribbons, we conducted second harmonic generation (SHG) micro-spectroscopy of our samples. It is known that 2H-MoS₂ bilayers exhibit low second order non-linear optical susceptibility due to inversion symmetry and their SHG signals are typically two orders of magnitude smaller than that of non-centrosymmetric monolayer MoS₂^{40,41}. In contrast, 3R-MoS₂ lacks inversion symmetry and exhibits intense SHG signals even in multilayer form⁴². Figure 4a and b show optical image and corresponding SHG intensity map of the homoepitaxially grown ribbons on monolayer MoS₂. While all the bilayer regions are uniform in contrast in the bright-field image, it is evident that different bilayer ribbons exhibit distinct non-linear optical response. Taking the SHG signals from the support monolayer as a reference (point 1 in Figure 4b), it can be seen that some ribbons exhibit (point 2) one order of

magnitude weaker SHG signals while others show nearly twice enhanced signals (point 3) (Supplementary Fig. 13). This quenching and enhancement of SHG signals can be attributed to 2H and 3R-type stacking of the ribbons, respectively, further verifying the epitaxial nature of the VLS growth. Figure 4c shows the SHG intensity map of a wide ribbon with predominantly 2H stacking based on average SHG intensity. The center region of the ribbon exhibits slightly enhanced signals, indicating weaker interlayer interactions. This observation is consistent with the STEM analysis that the symmetry and interlayer interaction vary over nanometer length scales in the center region of the ribbons due to strain and nanoripples (Figure 3g).

Mechanism of VLS growth of MoS₂ ribbons

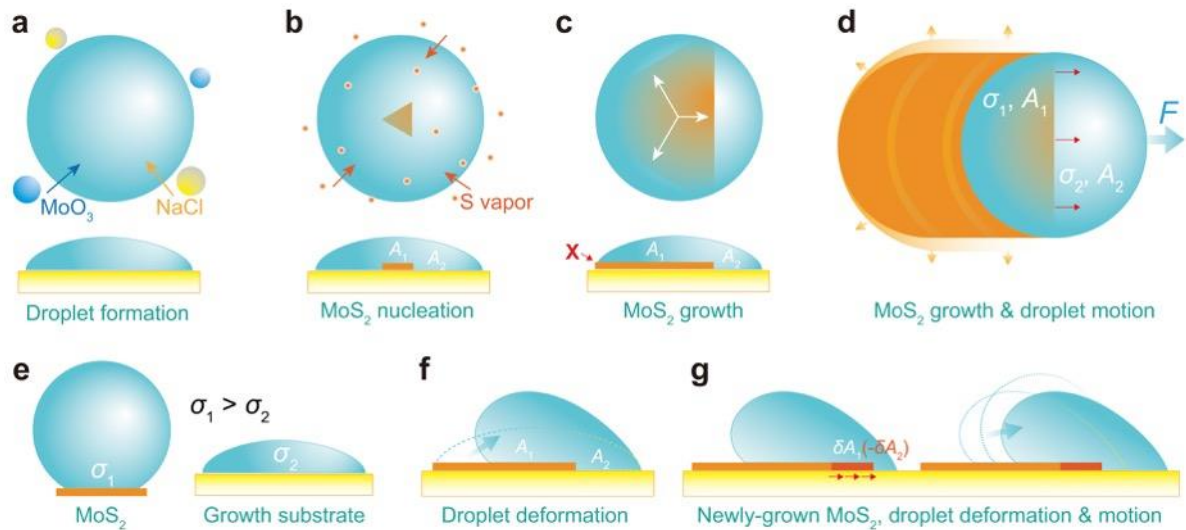


Figure 5 | Schematic illustration of the mechanism of ribbon formation. The VLS growth involves: (a) liquid droplet formation due to vapor phase reaction of MoO₃ and NaCl; (b) nucleation of MoS₂ flake at the droplet-substrate interface; (c) lateral growth of MoS₂ flake; (d) lateral horizontal displacement of the droplet and continuous growth of MoS₂ ribbon. (e) The droplet motion is induced by the interface energy difference between the droplet-MoS₂ ribbon (σ_1) and droplet-substrate (σ_2) interfaces. The droplet exhibits poorer wettability on MoS₂ ribbon than on growth substrate for $\sigma_1 > \sigma_2$. (f) De-wetting of droplet from “Position X” of Figure c to minimize the total interface free energy ($G_{\text{interface}}$), a quasi-equilibrium state is achieved. (g) Newly-grown MoS₂ ribbon leads to the increase of $G_{\text{interface}}$. The droplet rolls off the nanoribbon to minimize the $G_{\text{interface}}$ and restore the quasi-equilibrium state as illustrated in Figure f.

What drives the horizontal growth of predominantly monolayer MoS₂ ribbons? Here, we present our qualitative understanding of the growth processes and mechanism based on our experimental observations as schematically summarized in Figure 5. The precursor for VLS growth is the formed liquid droplets (Figure 5a) via reaction between the vapors of MoO₃ and NaCl as discussed above. When Na₂MoO₄ is used, liquid droplets form by direct melting (Supplementary Fig. 7). Subsequently, vaporized sulfur dissolves into the liquid droplet until saturation, triggering the formation of a MoS₂ nucleus at the droplet-substrate interface (Figure 5b). Continuous precipitation of MoS₂ allows commensurate growth on the support crystal structure (Figure 5c). As the MoS₂ ribbon growth proceeds, the liquid droplet begins to crawl on the substrate surface (Figure 5d). The origin of the crawling mode has been discussed in the literature but a unified theory has not been established due to complex kinetics of the processes involved^{43,44}. Here, we propose that the driving force for liquid droplet motion results primarily from the competition between the interface free energies of the droplet-MoS₂ ribbon (σ_1 , corresponding area A_1) and droplet-substrate (σ_2 , corresponding area A_2) (Figure 5e). With the condition of $\sigma_1 > \sigma_2$, the total interface free energy ($G_{\text{interface}}$) keeps increasing ($\delta G_{\text{interface}} = (\sigma_1 - \sigma_2)\delta A_1 > 0$) as the MoS₂ nucleation and growth at the droplet-substrate interface (Figure 5b and c). Then, the droplet de-wets MoS₂ ribbon form “Position X” of Figure 5c to minimize the $G_{\text{interface}}$ (shrinkage of A_1). As a result, a quasi-equilibrium state would be achieved as illustrated in Figure 5f. While the newly-grown MoS₂ ribbon further increases the area of higher-energy droplet-MoS₂ ribbon interface (σ_1) by δA_1 which means the $G_{\text{interface}}$ keeps increasing. The increased $G_{\text{interface}}$ leads to a driving force F for the droplet to displace laterally and restore the quasi-equilibrium state at the tip of the ribbon (Figure 5g). This is similar to the spontaneous lateral motion of a water droplet from a low to higher surface energy regions of the surface⁴⁵. While the magnitude of the interfacial energies is not known, finite difference in the surface energy of the ribbon and the substrate suggests that the above scenario is possible. The surface energy of NaCl is significantly greater than that of monolayer MoS₂^{46,47}, and similarly, monolayer MoS₂ on SiO₂/Si substrate is expected to exhibit higher surface energy compared to bilayer MoS₂⁴⁷. The different surface tensions of MoS₂ ribbon and growth substrates are well satisfied the condition of $\sigma_1 > \sigma_2$ which makes the motion of droplets possible during the continuous precipitation of MoS₂ from droplets. Other forces such as capillary and Marangoni forces may also play a role in the lateral motion⁴⁸. As the droplet crawls on the surface, sulfur and also possibly MoO₃ continue to dissolve into the

droplet inducing further continuous growth yielding the observed ribbon structures. The ripple-like features and local strains in the ribbons most likely resulted from the compressive stress induced by the droplet during growth. The predominance of monolayer growth may be explained by the fast motion of the liquid droplet, which allows limited time for the nucleation and growth of the second layer. Due to the finite vapor pressure of MoO_3 and S during growth, the ribbons can also grow at the edge of ribbons via vapor-solid (VS) or VSS conversion of the precursors. The strain-free edge region of the ribbons most likely resulted from such non-VLS growth (Figure 2d and Figure 5d).

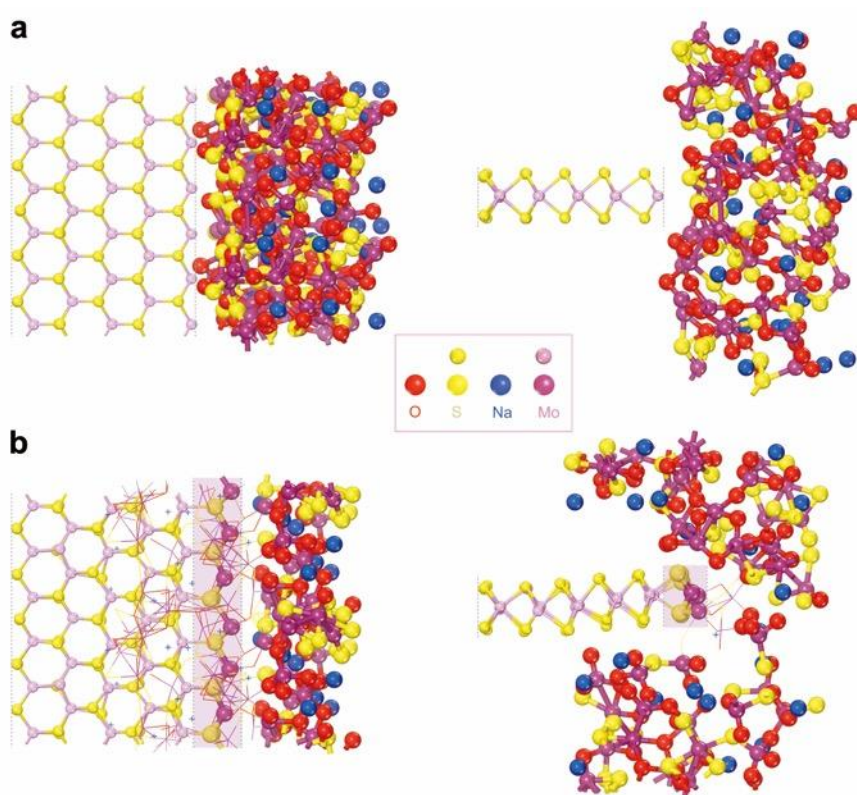


Figure 6 | Density functional theory based molecular dynamic (DFT-MD) simulation of MoS_2 precipitation process. (a) Initial state of the junction between S-rich Na-M-O droplet and adjacent MoS_2 nanoribbon. The left and right panels show the top and side view of the junction. (b) Mo and S atoms attach on the edge of MoS_2 nanoribbon, nearly completing a new row of atoms after annealing from 1500 to 1600 K for 17.5 ps (highlighted with a colored box).

In order to gain insight into the liquid-solid transformation, we performed density functional theory based molecular dynamic (DFT-MD) simulations of the precipitation process⁴⁹⁻⁵².

Initially, 22 Mo atoms and 43 S atoms were dissolved into a disordered $\text{Na}_{21}\text{Mo}_{21}\text{O}_{69}$ droplet, which was placed next to a MoS_2 nanoribbon with its Mo-terminated zigzag edge exposed to the droplet. The system was annealed from 1500 to 1600 K (see Method) in a period of ~ 17.5 ps. The initial and final structures are shown in Figure 6 (see Movie S1 and S2, Supplementary Information for the full animation). The simulation shows attachment of S and Mo to the zigzag edge, nearly completing a new row of MoS_2 . It is noteworthy that MoS_2 is not oxidized despite the presence of large number oxygen atoms. We also observe nucleation of MoS_2 clusters in regions that are rich of Mo/S atoms, further supporting the feasibility of liquid-mediated nucleation and growth of MoS_2 .

Conclusions

In summary, we have demonstrated the VLS growth of monolayer MoS_2 nano- and micro-ribbons on NaCl crystals and VLS-based homoepitaxy on monolayer MoS_2 using salt-assisted CVD. The VLS growth is made possible by liquid solution formation due to the vapor phase reaction between MoO_3 and NaCl. While there are some similarities with conventional VLS growth of nanowires and nanotubes, there are notable differences: the growth is strictly limited to the interface between the liquid phase precursor and the substrate surface; it yields predominantly monolayer products; and it is a van der Waals epitaxy. We envision that optimized VLS growth of 2D TMDs will allow rapid synthesis of nano- and micro-ribbon arrays and complex heterostructures that can be readily integrated into nanoelectronic and photonic devices. By identifying a suitable liquid phase intermediate compound, we believe that it will be possible to realize the direct 1D growth of a range of van der Waals layered materials. Our findings also open up avenues for the fundamental studies of lateral quantum confinement and dimensional crossovers in these 2D materials.

Methods

Salt-assisted VLS growth of MoS₂ ribbons: (1) For growing MoS₂ ribbons on NaCl crystals, a piece of freshly cleaved NaCl was placed above the MoO₃ powder on an alumina crucible. (2) For homoepitaxial ribbon growth, a SiO₂/Si substrate with pre-grown monolayer MoS₂ was loaded near the NaCl crystal. Sulfur was loaded in the low temperature upstream zone that reached ~230 °C during growth. 100 sccm Ar was used as carrier gas. The growth was conducted at 700-730 °C for 2-5 min. (See Supplementary Information for details)

STEM analysis of MoS₂ ribbons: STEM imaging was performed by using JEOL 2100F microscope equipped with a cold field emission gun operating at 60 kV and dodecapole correctors. The probe current is about 20-25 pA. The convergence semi-angle and the inner acquisition semi-angle are 35 mrad and 79 mrad.

SHG microscopy of homoepitaxially grown ribbons: An 800-nm femtosecond (fs) laser light with a repetition rate of 80 MHz and a duration of 140 fs delivered by a Ti: Sapphire oscillator (Coherent, Chameleon Ultra II) was focused on the MoS₂ samples using 100 air objective lens (NA = 0.90) of an inverted microscope (Nikon). The nonlinear optical signals generated by the MoS₂ samples were obtained by using the same objective lens and directed to a spectrometer (Princeton Instruments) for SHG spectroscopy or to a photomultiplier tube (PicoQuant, PMA 182) for SHG mapping. During mapping, the sample was raster scanned by a piezo-actuated 3D nano-positioning stage (Physik Instrumente).

DFT-MD calculation: The DFT-MD simulation were performed with the Vienna Ab Initio Simulation Package (VASP)⁴⁹. The exchange-correlation functional was described by the Perdew-Burke-Ernzerhof version of generalized gradient approximation⁵⁰ and the core region by the projector augmented wave method⁵¹. Considering the time-consuming nature of the DFT-MD, the plane-wave cutoff is set to be 300 eV and the Brillouin zone is sampled at Γ point only. All DFT-MD trajectories were run with the canonical ensemble (NVT) using a Nosé thermostat⁵² at the temperature from 1500 K (~ 6 ps), 1400 K (~ 3 ps) to 1600 K (~ 8.5 ps), which is higher than the real experimental temperature (~ 1000 K) but is necessary to accelerate the atomic evolution to observe a full annealing process in a short simulation time. The time step of the DFT-MD simulation is 2 fs. The total time scales of the trajectories are more than 17.5 ps. The unit cell used in the simulation has vacuum layer in the growth direction to avoid interaction between adjacent images and is periodic in another two directions. In the lattice used in simulations, initially the nanoribbon has three hexagons in the lateral direction and four

hexagons in the VLS-growth direction. The freestanding end of the nanoribbon is fixed during the simulation.

Acknowledgements

G.E. acknowledges Singapore National Research Foundation for funding the research under NRF Research Fellowship (NRF-NRFF2011-02) and medium-sized centre programme. G.E. also acknowledges support by Ministry of Education (MOE), Singapore, under AcRF Tier 2 (MOE2015-T2-2-123, MOE2017-T2-1-134). Y.L. and K.S. acknowledge the support from JSPS KAKENHI (JP16H06333). J. W. acknowledges the support from A*STAR IMRE/15-2C0111. F. D. acknowledges the support from the Institute for Basic Science (IBS-R019-D1). S.L. acknowledges Yang Sun for helpful discussion.

Author contributions

S.L. designed and conducted the VLS growth. Y.L. performed the STEM characterization of MoS₂ ribbons. S.L., J.W., Y.S., W.Z., F.D. and G.E. interpreted the VLS growth of MoS₂ ribbons. Z.W. and H.Z. performed the SHG mapping. S.L., J.W. and L.C. studied the Raman, PL, AFM and electrical properties of MoS₂ ribbons. S.L. and Q.Z. performed the TGA and XRD experiments. S.L. and Z.H. conducted the growth of MoX₂, WX₂ (X=S, Se, Te) from sodium molybdate and sodium tungstate. S.L., Y.L., W.Z., F. D. and G.E. wrote the paper. All the authors discussed and commented on the manuscript.

Competing financial interests

The authors declare no competing financial interests.

References

- 1 Shi, Y., Li, H. & Li, L.-J. Recent advances in controlled synthesis of two-dimensional transition metal dichalcogenides via vapour deposition techniques. *Chem. Soc. Rev.* **44**, 2744-2756 (2015).
- 2 Kang, K. *et al.* High-mobility three-atom-thick semiconducting films with wafer-scale homogeneity. *Nature* **520**, 656-660 (2015).
- 3 Chen, Y.-J., Cain, J. D., Stanev, T. K., Dravid, V. P. & Stern, N. P. Valley-polarized exciton-polaritons in a monolayer semiconductor. *Nat. Photon.* **11** 431-435 (2017)
- 4 Wachter, S., Polyushkin, D. K., Bethge, O. & Mueller, T. A microprocessor based on a two-dimensional semiconductor. *Nat. Commun.* **8** 14948 (2017).
- 5 Nie, Y. *et al.* First principles kinetic Monte Carlo study on the growth patterns of WSe₂ monolayer. *2D Mater.* **3**, 025029 (2016).
- 6 Van Der Zande, A. M. *et al.* Grains and grain boundaries in highly crystalline monolayer molybdenum disulphide. *Nat. Mater.* **12**, 554-561 (2013).
- 7 Najmaei, S. *et al.* Vapour phase growth and grain boundary structure of molybdenum disulphide atomic layers. *Nat. Mater.* **12**, 754-759 (2013).
- 8 Wu, S. *et al.* Vapor-solid growth of high optical quality MoS₂ monolayers with near-unity valley polarization. *ACS Nano* **7**, 2768-2772 (2013).
- 9 Li, S. *et al.* Halide-assisted atmospheric pressure growth of large WSe₂ and WS₂ monolayer crystals. *Appl. Mater. Today* **1**, 60-66 (2015).
- 10 Li, X. *et al.* Two-dimensional GaSe/MoSe₂ misfit bilayer heterojunctions by van der Waals epitaxy. *Sci. Adv.* **2**, e1501882 (2016).
- 11 Li, X. *et al.* Large-area synthesis of high-quality and uniform graphene films on copper foils. *Science* **324**, 1312-1314 (2009).
- 12 Kim, K. S. *et al.* Large-scale pattern growth of graphene films for stretchable transparent electrodes. *Nature* **457**, 706-710 (2009).
- 13 Zhang, Y., Zhang, L. & Zhou, C. Review of chemical vapor deposition of graphene and related applications. *Acc. Chem. Res.* **46**, 2329-2339 (2013).
- 14 Wang, S. *et al.* Shape evolution of monolayer MoS₂ crystals grown by chemical vapor deposition. *Chem. Mater.* **26**, 6371-6379 (2014).
- 15 Wagner, R. & Ellis, W. Vapor-liquid-solid mechanism of single crystal growth. *Appl. Phys. Lett.* **4**, 89-90 (1964).

- 16 Morales, A. M. & Lieber, C. M. A laser ablation method for the synthesis of crystalline semiconductor nanowires. *Science* **279**, 208-211 (1998).
- 17 Wu, Y. & Yang, P. Direct observation of vapor-liquid-solid nanowire growth. *J. Am. Chem. Soc.* **123**, 3165-3166 (2001).
- 18 Arenal, R., Stephan, O., Cochon, J.-L. & Loiseau, A. Root-growth mechanism for single-walled boron nitride nanotubes in laser vaporization technique. *J. Am. Chem. Soc.* **129**, 16183-16189 (2007).
- 19 Rosenfeld Hachon, Y., Popovitz-Biro, R., Grunbaum, E., Prior, Y. & Tenne, R. Vapor-liquid-solid growth of NiCl₂ nanotubes via reactive gas laser ablation. *Adv. Mater.* **14**, 1075-1078 (2002).
- 20 Yella, A. *et al.* Bismuth-catalyzed growth of SnS₂ nanotubes and their stability. *Angew. Chem. Int. Ed.* **48**, 6426-6430 (2009).
- 21 Peng, H. *et al.* Aharonov-Bohm interference in topological insulator nanoribbons. *Nat. Mater.* **9**, 225-229 (2010)
- 22 Geng, D. *et al.* Uniform hexagonal graphene flakes and films grown on liquid copper surface. *Proc. Natl. Acad. Sci. U.S.A.* **109**, 7992-7996 (2012).
- 23 Zavabeti, A. *et al.* A liquid metal reaction environment for the room-temperature synthesis of atomically thin metal oxides. *Science* **358**, 332-335 (2017).
- 24 Chen, J. *et al.* Chemical vapor deposition of large-size monolayer MoSe₂ crystals on molten glass. *J. Am. Chem. Soc.* **139**, 1073-1076 (2017).
- 25 Suzuki, H. *et al.* Wafer-scale fabrication and growth dynamics of suspended graphene nanoribbon arrays. *Nat. Commun.* **7**, 11797 (2016).
- 26 Ismach, A., Segev, L., Wachtel, E. & Joselevich, E. Atomic-step-templated formation of single wall carbon nanotube patterns. *Angew. Chem.* **116**, 6266-6269 (2004)
- 27 Tsivion, D., Schwartzman, M., Popovitz-Biro, R., von Huth, P. & Joselevich, E. Guided growth of millimeter-long horizontal nanowires with controlled orientations. *Science* **333**, 1003-1007 (2011).
- 28 Gong, Y. *et al.* Tellurium-assisted low-temperature synthesis of MoS₂ and WS₂ monolayers. *ACS Nano* **9**, 11658-11666 (2015).
- 29 Shen, Y. *et al.* Epitaxy-enabled vapor-liquid-solid growth of tin-doped indium oxide nanowires with controlled orientations. *Nano Lett.* **14**, 4342-4351 (2014).

- 30 Mudher, K. S., Keskar, M., Krishnan, K. & Venugopal, V. Thermal and X-ray diffraction studies on Na_2MoO_4 , $\text{Na}_2\text{Mo}_2\text{O}_7$ and $\text{Na}_2\text{Mo}_4\text{O}_{13}$. *J. Alloys Compd.* **396**, 275-279 (2005).
- 31 Johnson, D., Levy, J., Taylor, J., Waugh, A. & Brough, J. Purification of molybdenum: volatilisation processes using MoO_3 . *Polyhedron* **1**, 479-482 (1982).
- 32 Xia, Y. *et al.* One-dimensional nanostructures: synthesis, characterization, and applications. *Adv. Mater.* **15**, 353-389 (2003).
- 33 Gnanasekaran, T., Mahendran, K., Kutty, K. & Mathews, C. Phase diagram studies on the Na-Mo-O system. *J. Nucl. Mater.* **165**, 210-216 (1989).
- 34 Radisavljevic, B., Radenovic, A., Brivio, J., Giacometti, i. V. & Kis, A. Single-layer MoS_2 transistors. *Nat. Nanotech.* **6**, 147-150 (2011)
- 35 Splendiani, A. *et al.* Emerging photoluminescence in monolayer MoS_2 . *Nano Lett.* **10**, 1271-1275 (2010).
- 36 Mak, K. F., Lee, C., Hone, J., Shan, J. & Heinz, T. F. Atomically thin MoS_2 : a new direct-gap semiconductor. *Phys. Rev. Lett.* **105**, 136805 (2010).
- 37 Lin, J. *et al.* AC/AB stacking boundaries in bilayer graphene. *Nano Lett.* **13**, 3262-3268 (2013).
- 38 Kumar, N. *et al.* Second harmonic microscopy of monolayer MoS_2 . *Phys. Rev. B* **87**, 161403 (2013).
- 39 Malard, L. M., Alencar, T. V., Barboza, A. P. M., Mak, K. F. & de Paula, A. M. Observation of intense second harmonic generation from MoS_2 atomic crystals. *Phys. Rev. B* **87**, 201401 (2013).
- 40 Li, Y. *et al.* Probing symmetry properties of few-layer MoS_2 and h-BN by optical second-harmonic generation. *Nano Lett.* **13**, 3329-3333 (2013).
- 41 Jiang, T. *et al.* Valley and band structure engineering of folded MoS_2 bilayers. *Nat. Nanotech.* **9**, 825-829 (2014).
- 42 Zhao, M. *et al.* Atomically phase-matched second-harmonic generation in a 2D crystal. *Light Sci. Appl.* **5**, e16131 (2016).
- 43 Schwarz, K. W. & Tersoff, J. Multiplicity of steady modes of nanowire growth. *Nano Lett.* **12**, 1329-1332 (2012).
- 44 Zi, Y., Jung, K., Zakharov, D. & Yang, C. Understanding self-aligned planar growth of InAs nanowires. *Nano Lett.* **13**, 2786-2791 (2013).

- 45 Chaudhury, M. K. & Whitesides, G. M. How to make water run uphill. *Science*, 256, 1539-1541 (1992)
- 46 Bruno, M., Aquilano, D., Pastero, L. & Prencipe, M. Structures and surface energies of (100) and octopolar (111) faces of halite (NaCl): an ab initio quantum-mechanical and thermodynamical study. *Cryst. Growth Des.* **8**, 2163-2170 (2008).
- 47 Gaur, A. P. *et al.* Surface energy engineering for tunable wettability through controlled synthesis of MoS₂. *Nano Lett.* **14**, 4314-4321 (2014).
- 48 Wasan, D. T., Nikolov, A. D. & Brenner, H. Droplets speeding on surfaces. *Science* **291**, 605-606 (2001).
- 49 Kresse, G. & Furthmüller, J. Efficiency of ab-initio total energy calculations for metals and semiconductors using a plane-wave basis set. *Comput. Mater. Sci.* **6**, 15-50 (1996).
- 50 Perdew, J. P., Burke, K. & Ernzerhof, M. Generalized gradient approximation made simple. *Phys. Rev. Lett.* **77**, 3865 (1996).
- 51 Blöchl, P. E. Projector augmented-wave method. *Phys. Rev. B* **50**, 17953 (1994).
- 52 Nosé, S. A unified formulation of the constant temperature molecular dynamics methods. *J. Chem. Phys.* **81**, 511-519 (1984).

Supplementary Information for

Vapor-Liquid-Solid Growth of Monolayer MoS₂ Nanoribbons

Shisheng Li, Yung-Chang Lin, Wen Zhao, Jing Wu, Zhuo Wang, Zehua Hu, Youde Shen, Dai-Ming Tang, Junyong Wang, Qi Zhang, Hai Zhu, Leiqiang Chu, Weijie Zhao, Chang Liu, Zhipei Sun, Takaaki Taniguchi, Minoru Osada, Wei Chen, Qing-Hua Xu, Andrew Thye Shen Wee, Kazu Suenaga, Feng Ding and Goki Eda

Corresponding authors: g.eda@nus.edu.sg (G.E); shishengli1108@gmail.com (S.L.)

Chemical vapor deposition (CVD) of MoS₂ nanoribbons on NaCl crystals: The growth was conducted in ambient pressure with a movable tube furnace (MTI OTF-1200X, 20-mm-long heating zone) that allows rapid heating and cooling as illustrated in Supplementary Fig. 1a (Fast-heating CVD). A piece of freshly cleaved NaCl crystal (10×10×1 mm³, MTI) was placed on an alumina crucible (77/12/8 mm, L/W/H) with the cleaved surface faced down above MoO₃ powder (~5-10 mg, Alfa-Aesar) as illustrated in Supplementary Fig. 1b(I). The environmental humidity was kept lower than 50% to keep the NaCl surface dry without deliquescence. Sulfur (~30 mg) was loaded in the upstream region outside the heating zone (position 1, Supplementary Fig. 1a) during the temperature ramping process to keep it from evaporation. For a typical growth, 100 sccm Ar (99.995%) was pass through a 1000-mm-long and 50-mm-diameter (O.D.) quartz tube. The furnace temperature ramping rate is 25 °C/min. After the tube furnace reached the growth temperature (700-730 °C) and stabilized for ~2 min, the furnace was shifted to start the vaporization of sulfur and MoO₃ powder with the substrate at the centre of heating zone. The growth was terminated after ~2-5 min by moving the precursors and the substrate out of the heating zone and rapidly cooling to room temperature.

CVD of MoS₂ ribbons on monolayer MoS₂ film: For the epitaxial VLS growth of MoS₂ ribbons on monolayer MoS₂ film, a piece of NaCl crystal (10×10×1 mm³, MTI) and a piece of SiO₂/Si substrate with as-grown monolayer MoS₂ film were loaded on an alumina crucible as shown in Supplementary Fig. 1b(II). ~5-10 mg MoO₃ and ~30 mg sulfur (position 1, Supplementary Fig. 1a) were used as the source materials. Furthermore, ~10 mg sulfur (position 2, Supplementary Fig. 1a) was evaporated during the temperature ramping process to prevent the monolayer MoS₂ film from being oxidized. The optimized VLS epitaxial growth of MoS₂ ribbons on monolayer MoS₂ film was achieved with following recipe: Fast-heating CVD, ambient pressure, 100 sccm Ar (99.995 %), temperature ramping rate of 25 °C/min and hold at 700-730 °C for ~5 min (~2 min for stabilization, ~3 min for growth). KCl also works well as growth precursor as NaCl. In the case of KCl-assisted growth, the recipe is almost the same as the case of NaCl, and the optimal growth temperature is 675-700 °C.

Growth and characterization of monolayer MoS₂ film: ~0.5 ml of 0.2 mg/ml of NaCl aqueous solution was dropped in an alumina crucible (L/W/H: 77/12/8 mm). The crucible was baked on a hot plate at 120 °C until dry. Then, ~1 ml of 5 mg/ml MoO₃ aqueous suspension was dropped in the crucible and dried at 120 °C. A piece of SiO₂/Si substrate (NOVA), typical size of 20-25/12.5mm (L/W), was loaded on the crucible with polished face down. ~30 mg sulfur was loaded in the upstream, ~120 mm away from the center of the furnace. The fast-heating CVD was used for the growth of MoS₂ film. 100 sccm Ar (99.995%) was used as carrier gas. During the temperature ramping process (25 °C/min), the sulfur and crucible were kept at the low temperature. The center of the crucible is ~60 mm away from the center of the furnace. After the furnace reached the growth temperature (700 °C) and stabilized for ~2 min, the furnace was moved to heat the sulfur and crucible to initiate the growth of monolayer MoS₂ film for ~3 min. Finally, the growth was terminated by moving the precursors and the substrate out of the heating zone.

Sublimation of NaCl:

A piece of NaCl crystal (10×10×1 mm³, MTI) and a piece of SiO₂/Si substrate (NOVA) were loaded on an alumina crucible as shown in Supplementary Fig. 4a. The sublimation of NaCl crystal was performed at 700 °C in Ar for 10 min. Optical image shows a gradient of small NaCl crystals deposited on the SiO₂/Si substrate, suggesting sublimation of NaCl indeed

occurs below its melting point (801 °C). The surface of SiO₂/Si substrate was checked by SEM and EDX (Supplementary Fig. 4b-d).

Co-sublimation of NaCl and MoO₃

The sources, NaCl and MoO₃, were separated as shown in Supplementary Fig. 4e. The MoO₃ powder was loaded in the crucible under a piece of SiO₂/Si substrate. After annealing at 700 °C in Ar for 10 min, the surface of the SiO₂/Si substrate was checked by SEM and EDX (Supplementary Fig. 4f-h). “Liquid droplets” with elements of Na, Mo, O and Cl were observed indicating efficient reaction of NaCl and MoO₃.

Thermogravimetric (TG) study of pure MoO₃ and mixed MoO₃-NaCl: 11.64 mg MoO₃ powder and 34.46 mg mixed MoO₃-NaCl (20 wt%) were loaded in alumina crucibles for TG experiments, respectively. The TG experiments were carried out in N₂ atmosphere with a temperature ramping rate of 10 °C/min to 1000 °C. The TG-DTG data and optical images of the crucibles after the TG experiments are showing in Supplementary Fig. 5a and b.

In-situ observation of the melting of mixed MoO₃-NaCl: ~60 mg mixed MoO₃-NaCl was loaded in a clean alumina crucible. Typical CVD process without sulfur was performed. Photos were taken at room temperature (R.T.), 400 °C, 530 °C, 600 °C and 700 °C, respectively (Supplementary Fig. 5c). The white alumina crucible is “stained” at 530 °C indicating the release of vapor phase product. This matches well with our TG-DTG data. At 600 °C and above, the melting of the reaction products and wetting of the bottom of alumina crucible were directly observed (Supplementary Fig. 5c).

X-ray diffraction (XRD) of the reaction product of mixed MoO₃-NaCl: To prepare XRD sample, ~200 mg mixed MoO₃-NaCl was loaded in a clean alumina crucible. After annealing at 700 °C in Ar for 20 min. The reaction product was collected for XRD (Supplementary Fig. 5d). XRD pattern shows that reaction product is a mixture of Na₂Mo₂O₇ and residual NaCl.

Regrowth of MoS₂ from the reaction product of mixed MoO₃-NaCl: The obtained mixture of Na₂Mo₂O₇ and residual NaCl was dispersed on a SiO₂/Si substrate for growing MoS₂. The

as-grown MoS₂ shows a morphology of “coffee-ring” indicating the melting of the Na₂Mo₂O₇ during the formation of MoS₂ (Supplementary Fig. 5e-g).

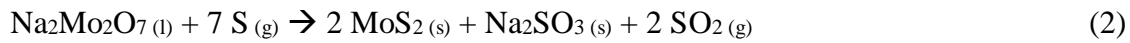
The chemical composition of the liquid droplets for VLS growth: For the NaCl-assisted growth of MoS₂ ribbons on monolayer MoS₂ at 700 °C, the growth was terminated within 1 min to preserve the liquid droplets at the end of ribbons (Supplementary Fig. 6a-f). The EDX spectra of these liquid droplets reveal the existence of elements of Mo, S, Na, O and trace amount of Cl which matches well with our XRD data (Supplementary Fig. 5d). Similarly, the slow growth of MoS₂ ribbons was also achieved with KCl as precursor at a lower growth temperature (675 °C). The trace at the tails of the MoS₂ ribbons clearly demonstrate the melting of the particles (Supplementary Fig. 6g and h). EDX spectra of the particles at the heads confirmed the existence of elements of Mo, S, K, O and trace amount of Cl (Supplementary Fig. 6i).

Thus, we conclude that the liquid droplets for growing MoS₂ ribbons is mainly a compound of Na/K, Mo and O. Cl may also contribute in lowering the melting point of the mixture. However, it is likely that Cl is lost quickly in gas phase MoO₂Cl₂¹ during growth.

Possible chemical reaction route: Based on the above analysis, we deduced the possible VLS growth process as following. During the temperature ramping to the growth temperature of 700-730 °C, the co-sublimated MoO₃ and NaCl first react as equation (1)¹.



Then, sulfur vapor dissolved into the liquid-phase Na₂Mo₂O₇. Finally, monolayer MoS₂ nanoribbons were grown on the substrate.



Growth of MoS₂ ribbons with patterned Na₂MoO₄ precursor on sapphire substrates: To prepare patterned Na₂MoO₄, sapphire substrates with line patterns on photoresist were fabricated by photolithography. Then, ~1 ml of 20 mg/ml Na₂MoO₄ aqueous solution was spin-coated on the sapphire substrates. A standard lift-off process was employed to remove photoresist. The as-fabricated substrates with Na₂MoO₄ line patterns were used for the growth of MoS₂ ribbons. The growth was done at 700 °C in 100 sccm Ar for ~5 min (Supplementary Fig. 7)

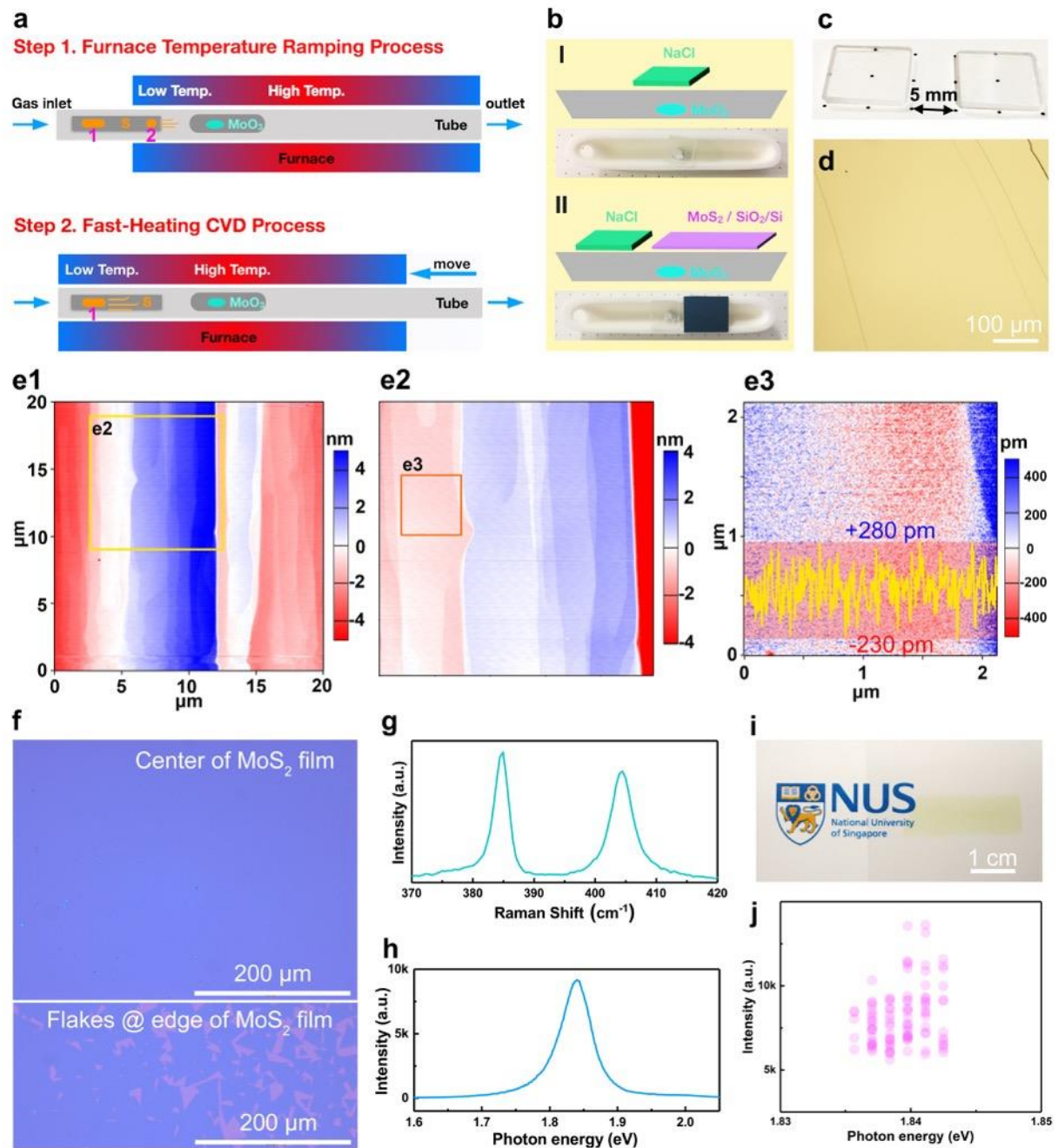
VLS growth of monolayer MoX₂ and WX₂ (X = S, Se, Te) crystals from Na₂MoO₄ and Na₂WO₄ precursors: For the growth of MoX₂ (X = S, Se), 2 mg/ml Na₂MoO₄ (T_m = 687 °C) aqueous solution was spin-coated on sapphire (Namiki Precision) or SiO₂/Si substrates (Nova). The optimized growth condition for MoX₂ (X = S, Se) is 700-725 °C in Ar for ~5 min. For the growth of MoTe₂ and WX₂ (X = S, Se, Te), 2 mg/ml NaMoO₄ or Na₂WO₄ (T_m = 698 °C) aqueous solution was spin-coated on sapphire or SiO₂/Si substrates, respectively. The optimized growth condition for MoTe₂ and WX₂ (X = S, Se, Te) is 725-775 °C in Ar/H₂ (5%) for ~5 min. For the growth of MoS₂/MoSe₂ heterostructure, CVD-grown monolayer MoS₂ crystals were wet-transferred on a new SiO₂/Si substrate first. Then, 2 mg/ml Na₂MoO₄ aqueous solution was spin-coated on the SiO₂/Si substrate. MoSe₂ monolayers were grown at 725 °C for MoS₂/MoSe₂ heterostructure. Supplementary Fig. 8c-j show the morphology of monolayer MoX₂, WX₂ (X = S, Se, Te) crystals and MoS₂/MoSe₂ heterostructure grown with Na₂MoO₄ and Na₂WO₄ precursors, respectively. All the growth was conducted in a 2-inch (O.D.) tube furnace with a total flow rate (Ar, Ar/H₂) of 100 sccm.

Large-area growth of monolayer MoS₂ ribbons with Na₂MoO₄ precursor on sapphire substrates: For the growth of MoS₂ ribbons, ~2 ml of 4 mg/ml Na₂MoO₄ aqueous solution was spin-coated on a 2-inch sapphire wafer (Namiki Precision). The growth was conducted in a 2-inch tube furnace. The optimized growth condition is at ~700-775 °C in 100 sccm Ar for ~2-5 min (Supplementary Fig. 8k and l)

Large-area uniform growth of monolayer MoS₂ film with Na₂MoO₄ precursor on sapphire substrates: For the growth of monolayer MoS₂ film, ~4 ml of 20 mg/ml Na₂MoO₄ aqueous solution was spin-coated on a 2-inch sapphire wafer. The growth was conducted in a 3-inch tube furnace. The optimized growth condition is at 725 °C in 200 sccm Ar for ~5 min (Supplementary Fig. 8m and n).

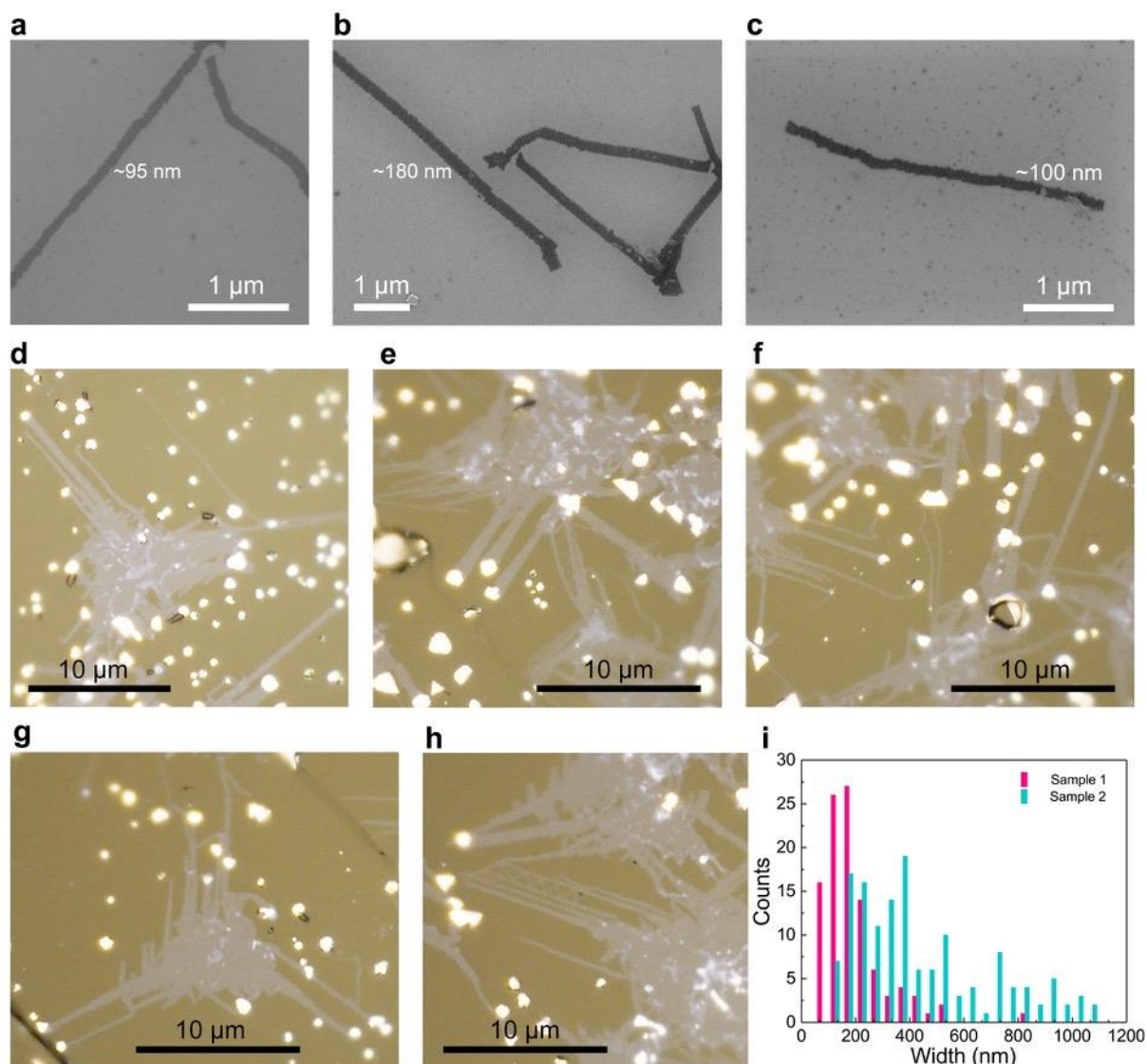
Wet transfer of monolayer MoS₂ nanoribbons from NaCl crystal: A layer of PMMA film was spin-coated on the NaCl crystal with as-grown monolayer MoS₂ nanoribbons (PMMA solution: 950K-5%, 3000 rpm, 60 s). The NaCl crystal was removed by simply dissolving it in DI water.

Field effect transistor fabrication and measurement: Standard e-beam lithography patterning and lift-off procedures were performed to define the electrodes. 2 nm Cr and 50 nm Au film was deposited as electrodes by thermal evaporator. Electrical measurements were conducted in N₂-filled glovebox at room temperature. The applied source-drain bias (V_{ds}) is 1 V. All the transport curves are presented in effective 2D electrical conductivity, $\sigma = (I_{ds}/V_{ds})*(L/W)$, where the I_{ds} is source-drain current, L and W are the channel length and width, respectively. From the linear regime of the transfer curves, the field-effect mobility was calculated using the equation $\mu = (1/C_{ox})(d\sigma/dV_{bg})$, where C_{ox} is the area capacitance of the gate oxide (1.2×10^{-4} F/m² for 285 nm SiO₂), V_{bg} is the back-gate bias.

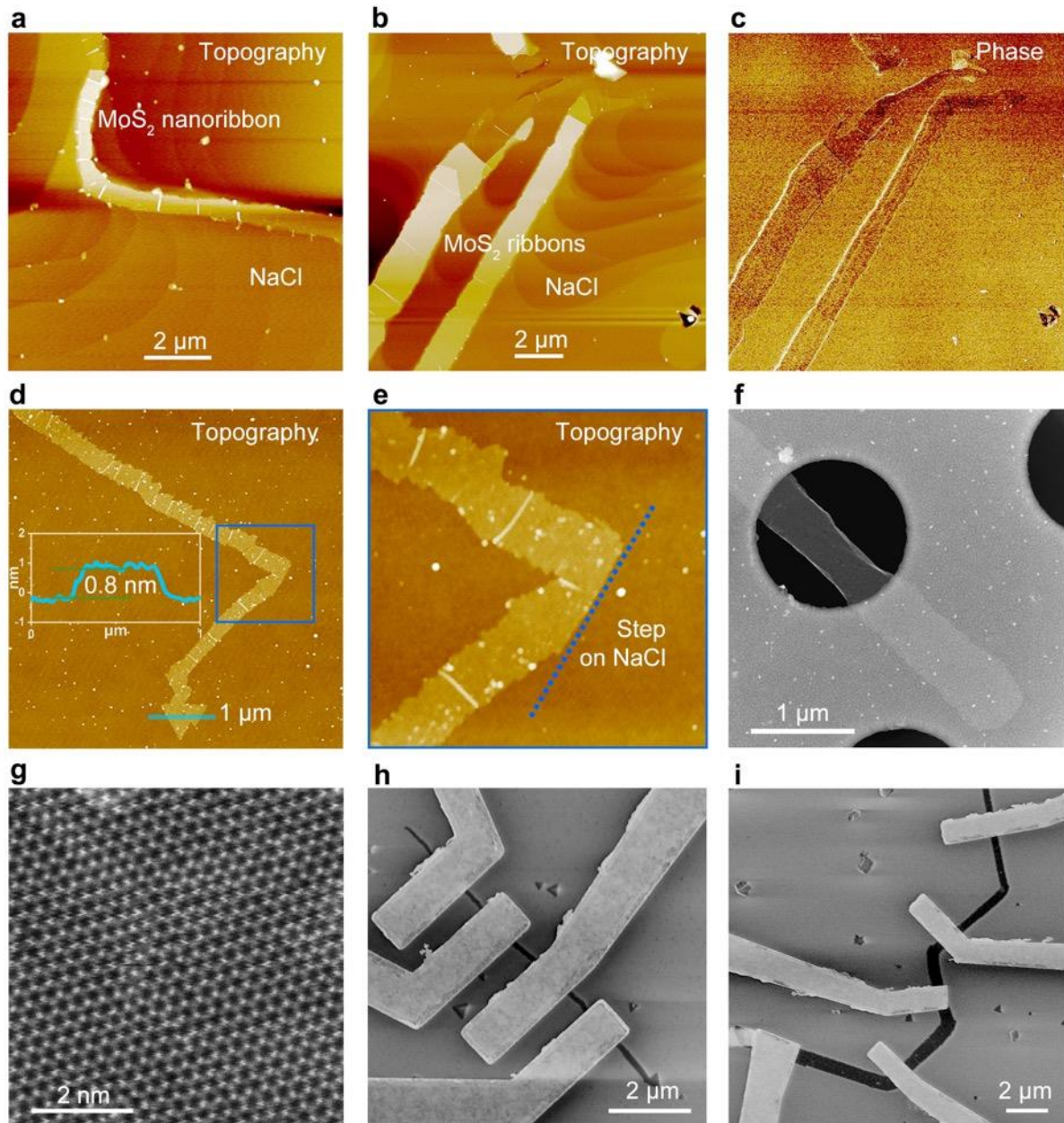


Supplementary Figure 1 | Schematic illustration of fast-heating CVD process and characterization of the raw materials for VLS growth of MoS₂ ribbons. (a) Schematic illustration of the fast-heating CVD process. (b) Schematic illustrations and optical images showing the configurations for growth of MoS₂ ribbons on (I) NaCl crystal and (II) monolayer MoS₂ film. (c) Photograph of two freshly cleaved NaCl crystals. (d) Optical image of the surface of a freshly cleaved NaCl crystal. (e1-e3) AFM images showing the surface of NaCl crystal with parallel surface steps. The flat surface has a roughness of approximately 0.5 nm. (f) Optical images of monolayer MoS₂ film and flakes grown on a SiO₂/Si substrate used

for the homoepitaxial growth of MoS₂ ribbons. (g, h) Typical Raman and PL spectra of monolayer MoS₂ film. (i) Optical image of a transferred monolayer MoS₂ film on PET substrates. (j) The PL peak energy and intensity distribution of a monolayer MoS₂ film. 100 PL spectra were collected from the whole surface of a monolayer MoS₂ film ($\sim 2.5 \times 1 \text{ cm}^2$).

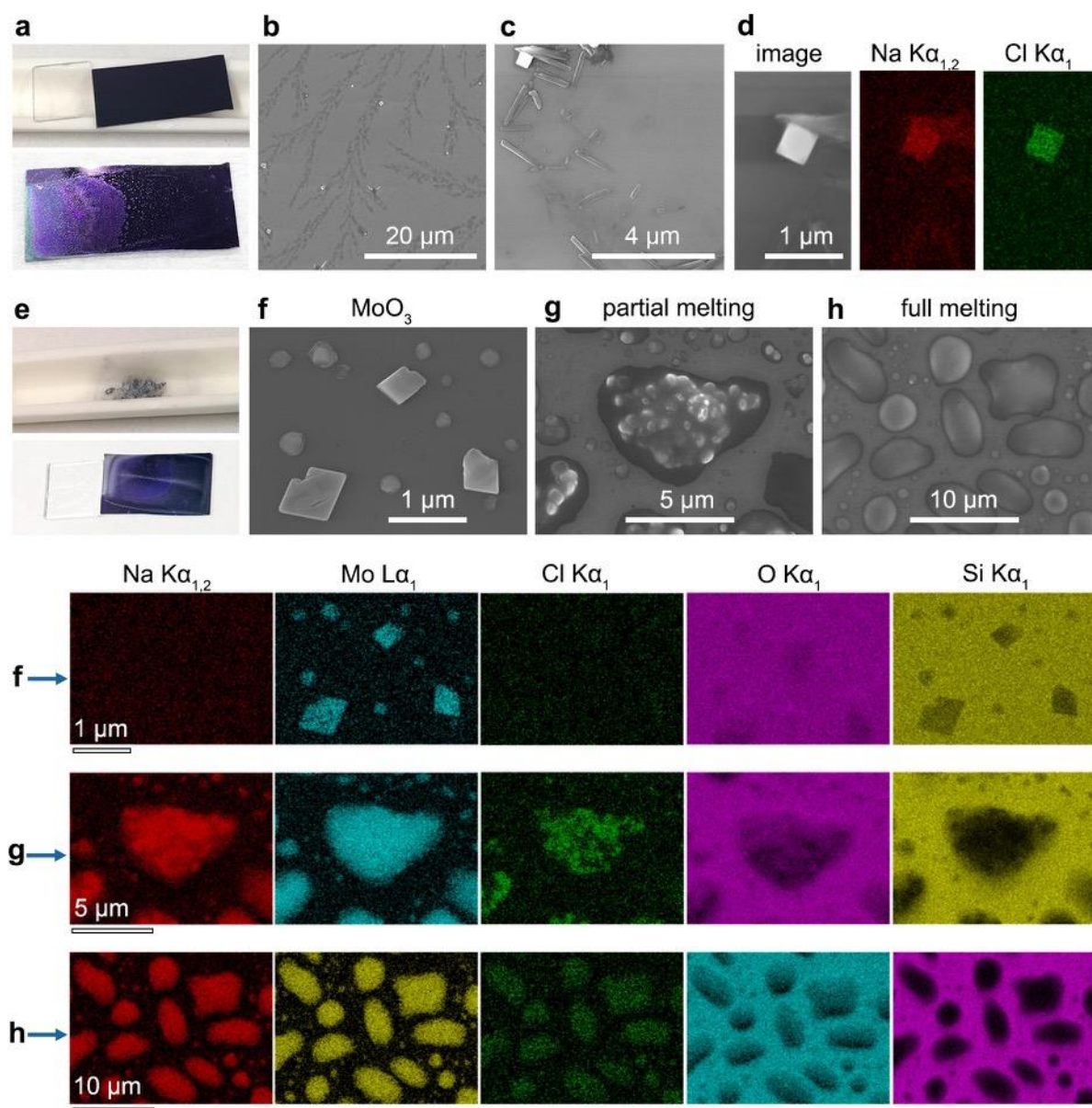


Supplementary Figure 2 | Width distribution of MoS₂ nanoribbons grown on NaCl crystal. (a-c) SEM and (d-h) optical images of MoS₂ nanoribbon structures. (i) Histogram showing the width distribution of >100 nanoribbons in two samples. (a-c) MoS₂ nanoribbons grown with $\sim 1 \text{ mg}$ MoO₃ powder, the average nanoribbon width is $\sim 195 \text{ nm}$. (d-h) MoS₂ nanoribbons grown with $\sim 20 \text{ mg}$ MoO₃ powder, the average nanoribbon width is $\sim 440 \text{ nm}$.



Supplementary Figure 3 | Morphology of as-grown and transferred monolayer MoS₂ ribbons. (a, b) AFM topography images of MoS₂ ribbons grown on NaCl crystal. (c) Corresponding phase image of (b). (d) AFM topography image of a transferred MoS₂ nanoribbon on SiO₂/Si substrate. (e) AFM topography image of a MoS₂ nanoribbon showing the details around the kink that correspond to the step on NaCl crystal surface. This morphology suggests that the migration of the liquid droplet was obstructed by the NaCl surface step and the growth direction was changed therefore. (f) A TEM image showing a general view of a MoS₂ nanoribbon on a TEM grid. (g) A high-resolution STEM image of MoS₂ nanoribbon indicating its high crystallinity. (h, i) SEM images of (h) straight and (i)

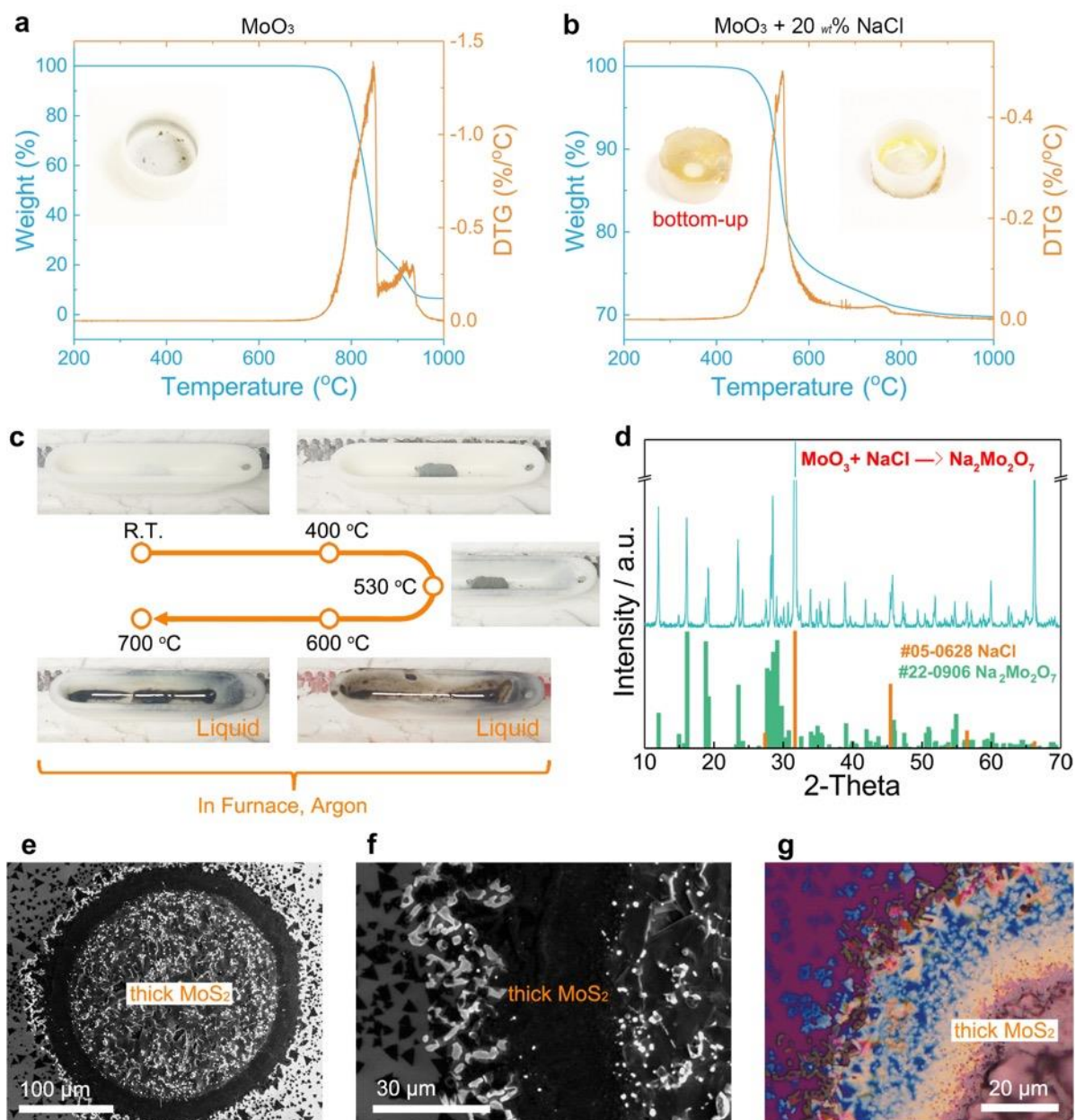
kinked MoS₂ nanoribbon devices. The width of the narrowest segment of the straight nanoribbon is ~60 nm.



Supplementary Figure 4 | Sublimation of NaCl and co-sublimation of NaCl and MoO₃.

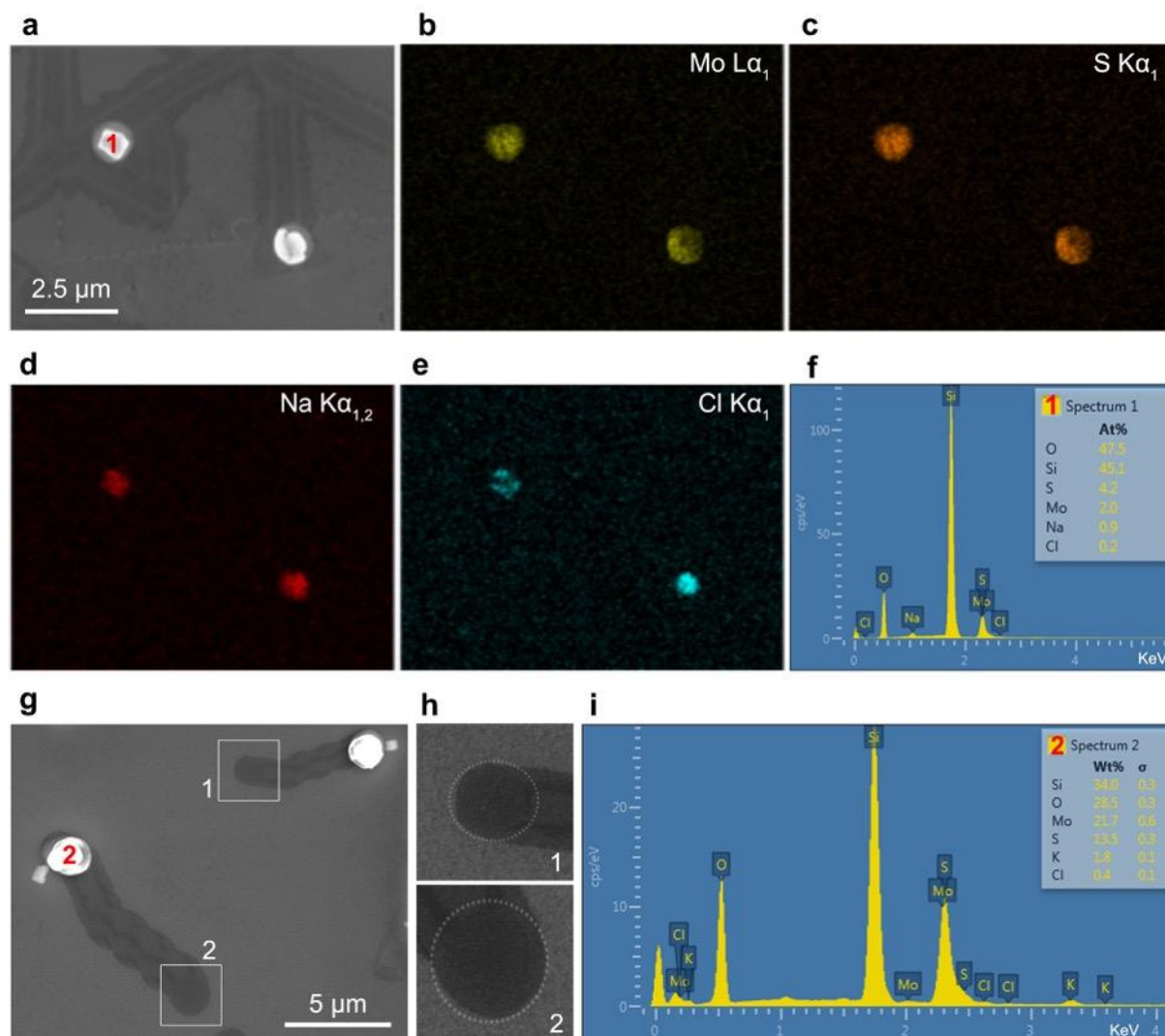
(a) Optical image of the sublimed NaCl on a clean SiO₂/Si substrate at 700 °C in Ar. (b, c) SEM images of NaCl crystals deposited on the SiO₂/Si substrate. (d) SEM image and corresponding EDX mapping images of Na K $\alpha_{1,2}$ and Cl K α_1 . (e) Optical image of co-sublimated NaCl and MoO₃ on a clean SiO₂/Si substrate at 700 °C in Ar. (f-h) SEM images and corresponding EDX mapping images (Na K $\alpha_{1,2}$, Mo L α_1 , Cl K α_1 , O K α_1 and Si K α_1) of (f) MoO₃, (g) partially and (h) fully liquefied reaction products of mixed MoO₃-NaCl,

respectively. Samples shown in (g) and (h) contain low-melting-point $\text{Na}_2\text{Mo}_2\text{O}_7$ and residual NaCl .



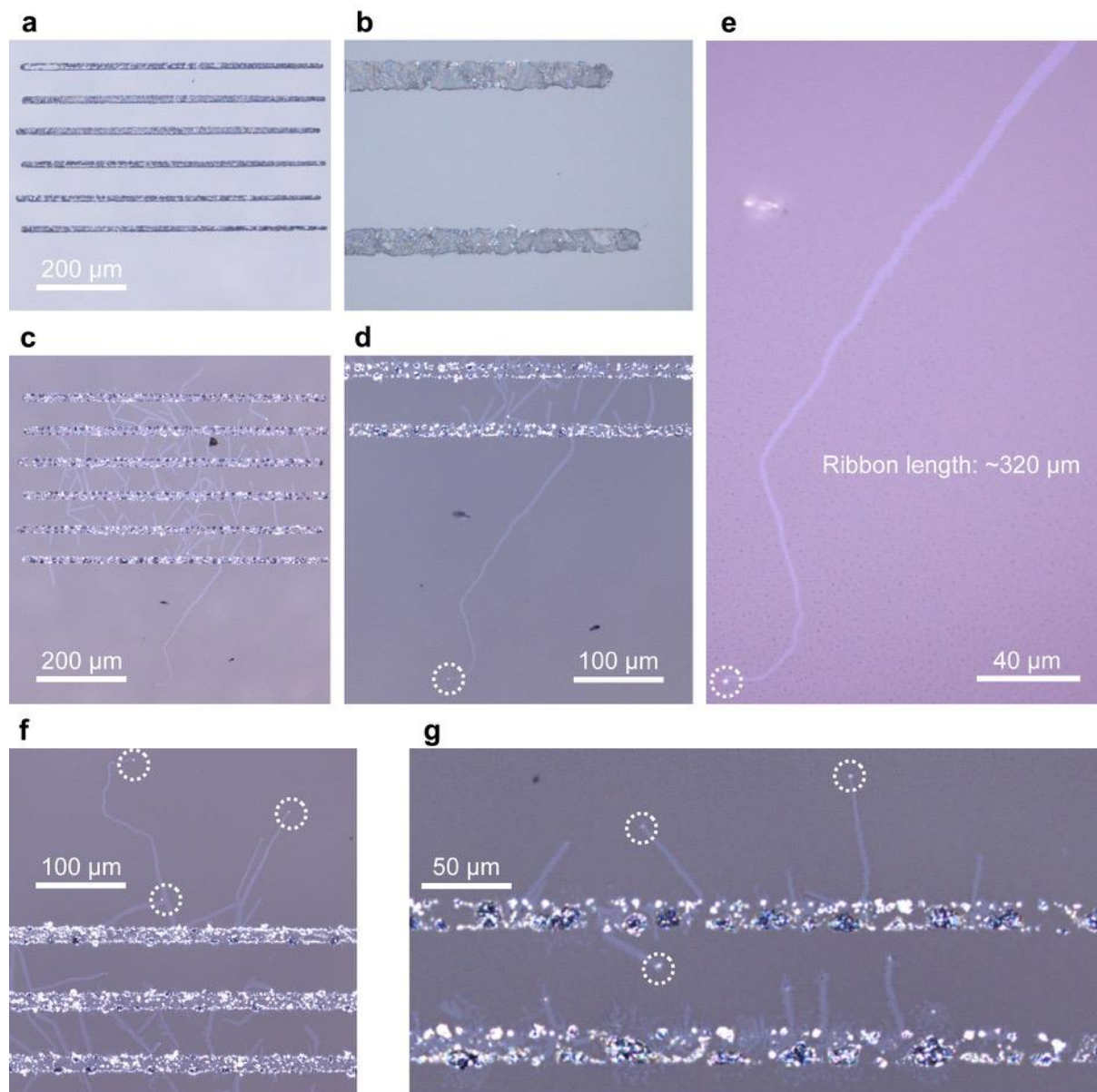
Supplementary Figure 5 | Reaction of MoO_3 - NaCl mixture. (a, b) TG-DTG curves of (a) MoO_3 and (b) mixed MoO_3 - NaCl in N_2 with a temperature ramping rate of 10 °C/min. Insets are optical images showing the residuals in and out alumina crucibles after TG study. (c) Optical images showing melting of MoO_3 - NaCl mixture when heated to 600 °C and above in Ar. (d) XRD pattern of the reaction product of MoO_3 - NaCl mixture at 700 °C. It contains $\text{Na}_2\text{Mo}_2\text{O}_7$ and residual NaCl . (e, f) SEM and (g) optical images of MoS_2 obtained by

sulfurization of $\text{Na}_2\text{Mo}_2\text{O}_7$. The “coffee-ring” pattern suggests that the precursors were in a liquid state during the growth.

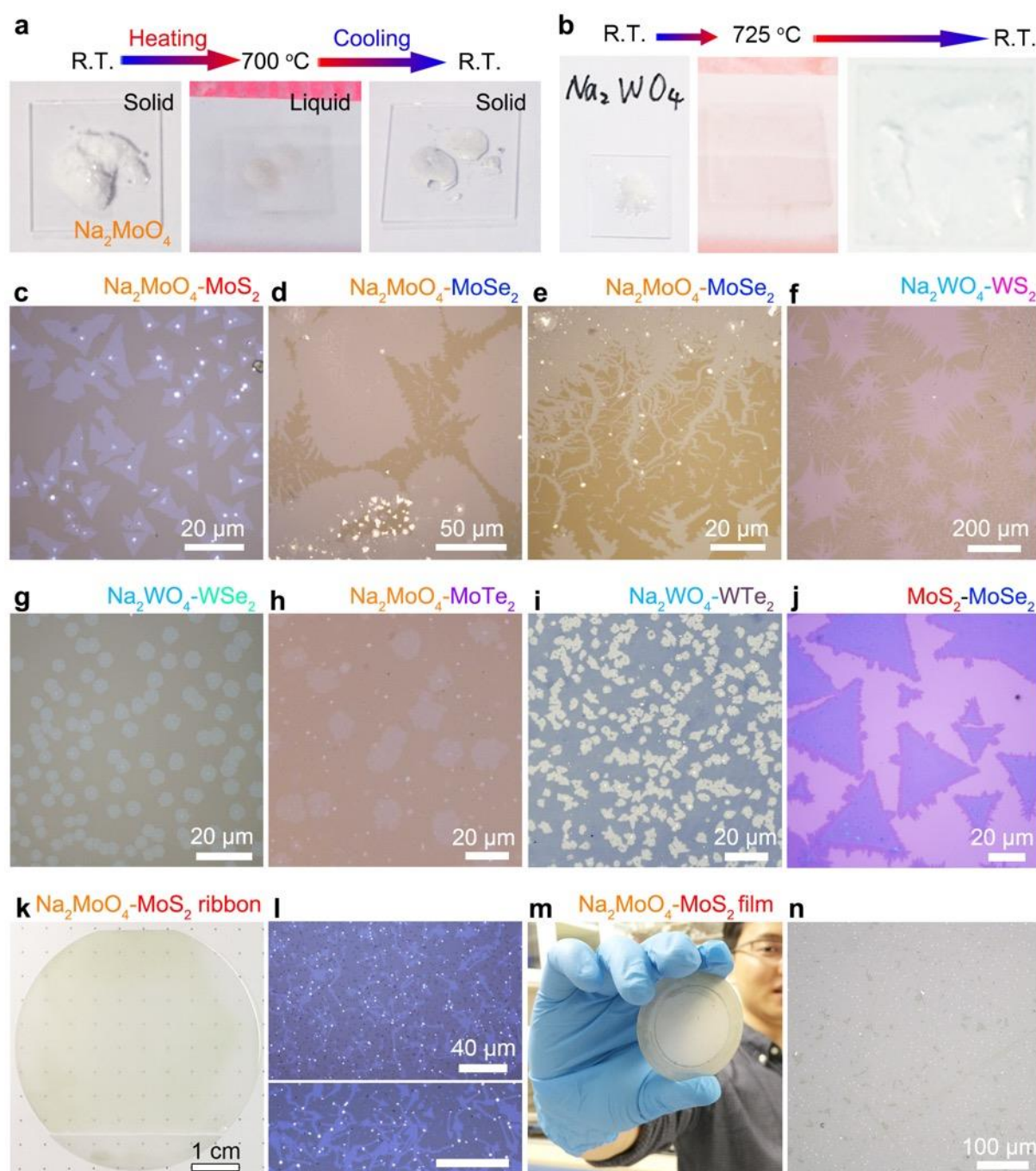


Supplementary Figure 6 | SEM/EDX analysis of the particles terminating MoS_2 ribbons.

(a) SEM image of two particles terminating two MoS_2 ribbons grown on monolayer MoS_2 film. (b-e) Corresponding EDX element mapping images of (a): (b) $\text{Mo L}\alpha_1$, (c) $\text{S K}\alpha_1$, (d) $\text{Na K}\alpha_{1,2}$ and (e) $\text{Cl K}\alpha_1$. (f) EDX spectrum of the particle 1. (g-i) KCl-assisted growth of MoS_2 ribbons on monolayer MoS_2 film (675 °C). (g) SEM image shows the heads and tails of two short MoS_2 ribbons. (h) The morphology of the tail region the ribbons (the end that is not terminated by a particle). The round feature is indicative of the liquid-state of the particle during the growth. (i) EDX spectrum of the particle 2 which contains elements of Mo, S, K, O and small amount of Cl.



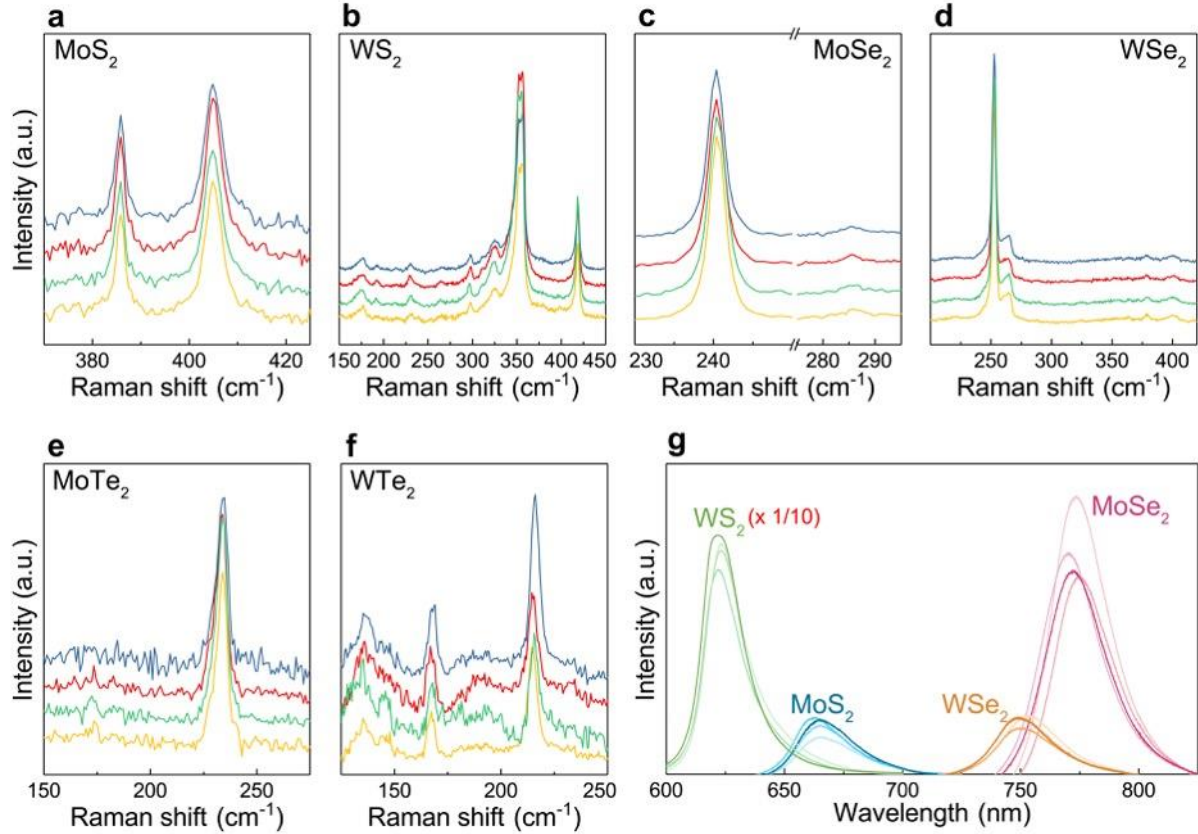
Supplementary Figure 7 | VLS growth of MoS₂ ribbons with patterned Na₂MoO₄ precursor. (a, b) Optical images of patterned Na₂MoO₄ lines. (c-g) Optical images of the as-grown ribbons. The ribbon width reduction reflects gradual consumption of Mo from liquid Na₂MoO₄ droplet during growth. The bright dots terminating individual ribbons are circled. They indicate that the ribbons were grown from “liquid catalyst” in VLS mode.



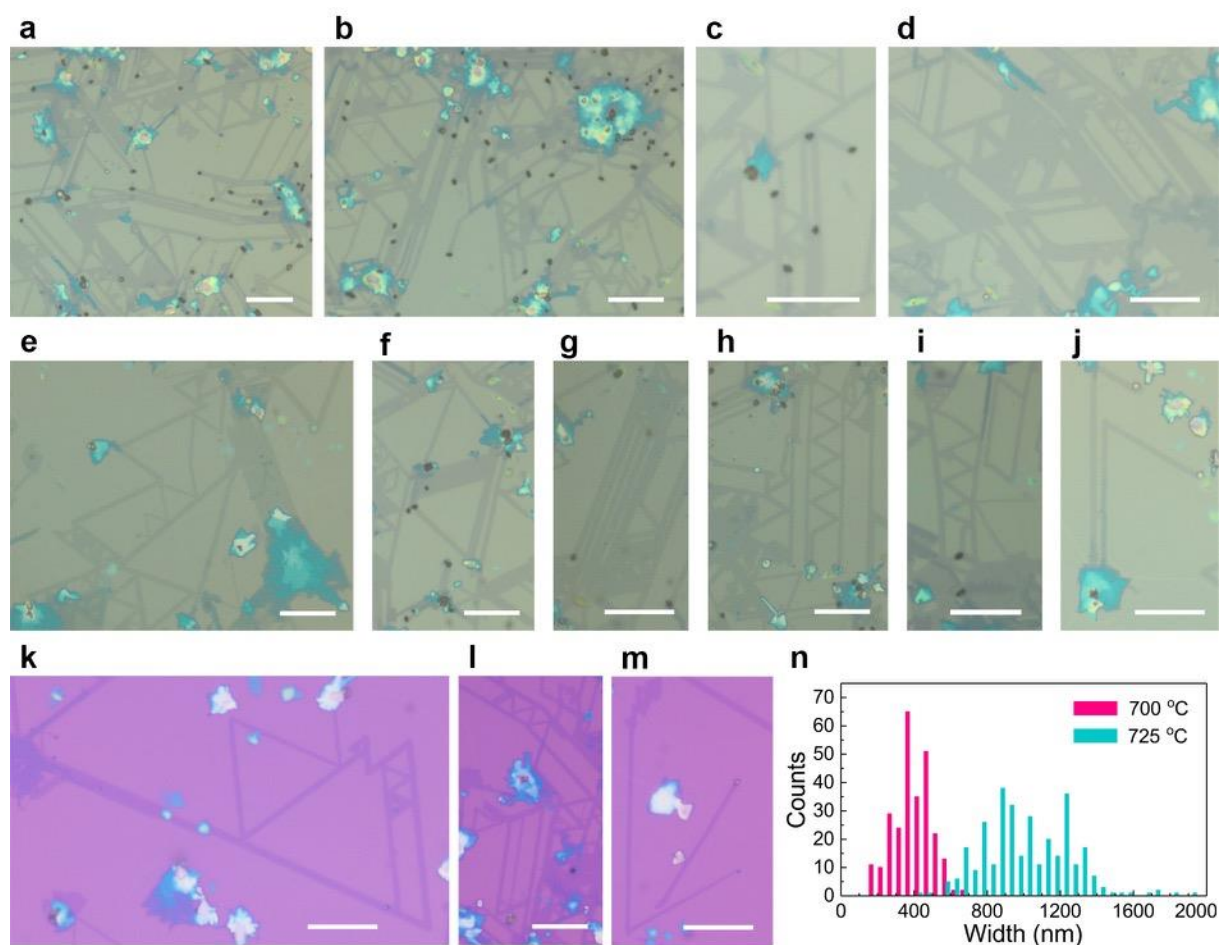
Supplementary Figure 8 | Growth of TMDs with Na_2MoO_4 and Na_2WO_4 as precursors.

(a) Direct observation of the melting of Na_2MoO_4 when annealing at 700 °C in Ar. (b) Direct observation of the melting of Na_2WO_4 when annealed at 725 °C in Ar. (c) Optical image of monolayer MoS_2 crystals grown with Na_2MoO_4 at 700 °C in Ar. (d, e) Optical images of monolayer MoSe_2 crystals grown with Na_2MoO_4 at 725 °C in Ar. (f, g) Optical images of monolayer (f) WS_2 and (g) WSe_2 crystals grown with Na_2WO_4 at 750 °C in Ar/H_2 (5%), respectively. (h, i) Optical image of monolayer (h) MoTe_2 , (i) WTe_2 crystals grown with

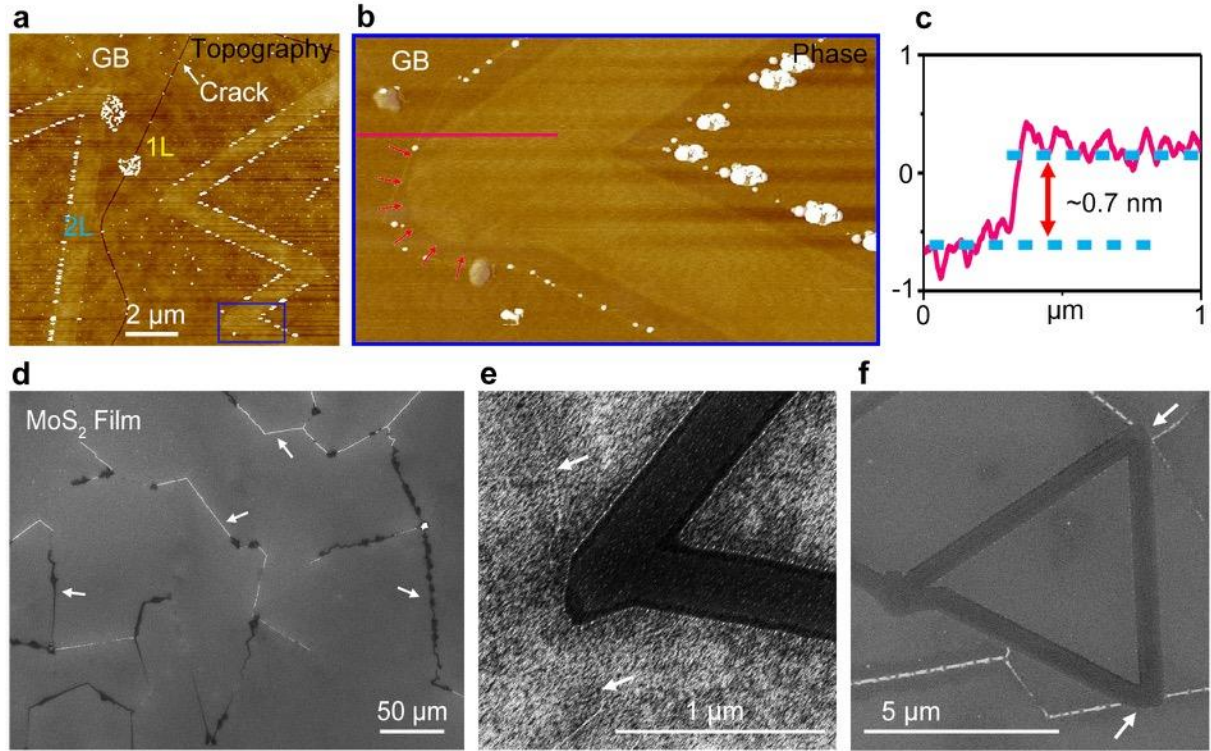
Na_2MoO_4 and Na_2WO_4 at 750 °C in Ar/H_2 (5%), respectively. (j) Optical image of $\text{MoS}_2/\text{MoSe}_2$ heterostructure grown with Na_2MoO_4 at 725 °C for MoSe_2 on monolayer MoS_2 flakes. (k, l) Growth of MoS_2 ribbons on 2-inch sapphire substrate with Na_2MoO_4 at 775 °C. (m, n) Growth of MoS_2 film on 2-inch sapphire substrate with Na_2MoO_4 at 725 °C.



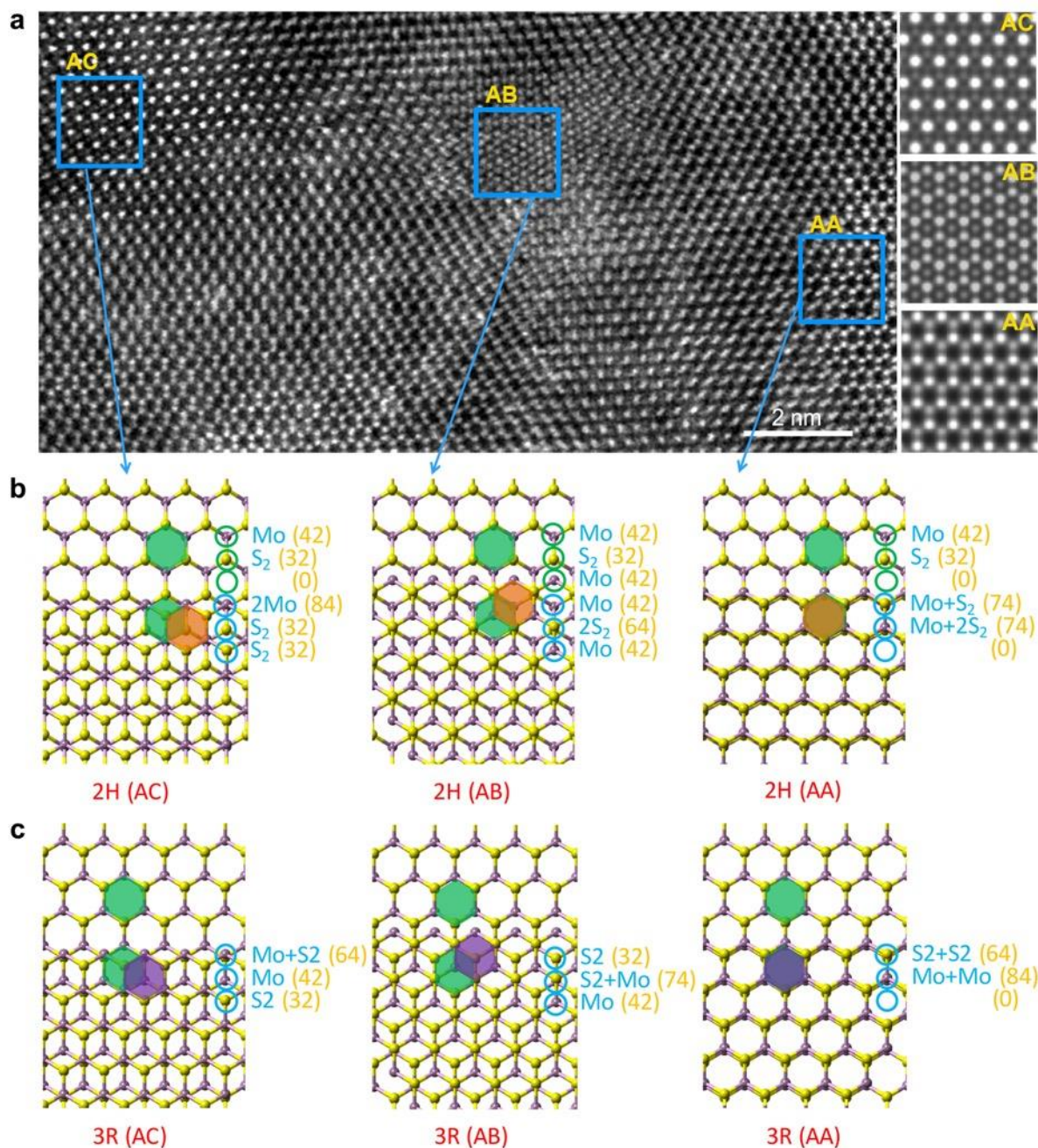
Supplementary Figure 9 | Raman and PL spectra of as-grown TMDs with Na_2MoO_4 and Na_2WO_4 as precursors. Raman spectra of as-grown (a) MoS_2 , (b) WS_2 , (c) MoSe_2 , (d) WSe_2 , (e) MoTe_2 , (f) WTe_2 . (g) PL spectra of WS_2 , MoS_2 , WSe_2 and MoSe_2 monolayers.



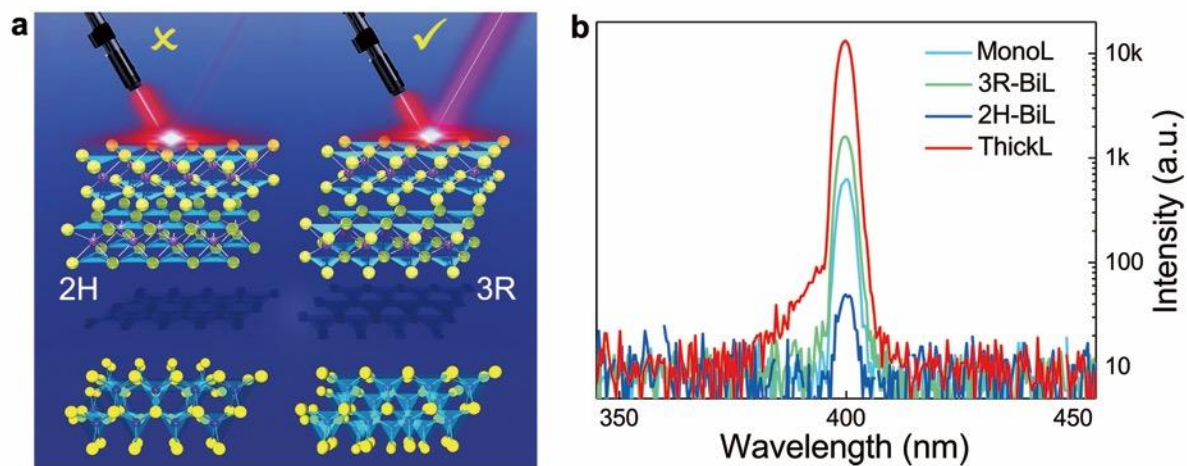
Supplementary Figure 10 | Optical images of MoS₂ ribbons and islands grown on monolayer MoS₂. All the samples were grown on MoS₂/SiO₂ (285 nm)/Si substrates. Figures a-j show different colors due to the cover of a PMMA layer. The scale bar is 10 μ m. (n) Width distribution of as-grown MoS₂ ribbons. The MoS₂ nanoribbons grown at 700 °C have an average width of ~400 nm. The MoS₂ ribbons grown at 725 °C have an average width of ~1020 nm.



Supplementary Figure 11 | MoS₂ ribbon kinks and the GBs of the monolayer MoS₂. (a) AFM topography image of two MoS₂ ribbons grown on two adjacent MoS₂ grains separated by a grain boundary (GB). (b) AFM phase image showing the kink region. (c) The height profile along the red line in (b). The step height of ~0.7 nm indicates that the MoS₂ ribbon is monolayer. (d) SEM image revealing line features appearing at the GBs of a monolayer MoS₂ film. (e) SEM image showing kinks of MoS₂ ribbons coinciding with the GBs. (f) GBs after partially etching with H₂O vapor. The line features of GBs are more clearly visible.



Supplementary Figure 12 | ADF-STEM analysis of the center of a MoS₂ nanoribbon grown on monolayer MoS₂. (a) STEM image showing spatially varying stacking sequence in the center region of a 2H-dominated MoS₂ nanoribbon. (b, c) Schematic illustration of AC, AB and AA stacking sequence in (b) 2H-type and (c) 3R-type MoS₂ nanoribbons. The number correspond to the expected ADF-STEM intensity variations. The ADF-STEM intensity variations in (a) are consistent with the variation expected in 2H-type stacking with relative displacement of the layers.



Supplementary Figure 13 | SHG of MoS₂ nanoribbons grown on monolayer MoS₂. (a) Schematic illustration of SHG of bilayer 2H- and 3R-MoS₂. (b) SHG spectra of monolayer MoS₂, bilayer 2H- and 3R-MoS₂ nanoribbons and thick MoS₂ islands.

Reference

1. Johnson, D., Levy, J., Taylor, J., Waugh, A. & Brough, J. Purification of molybdenum: volatilisation processes using MoO₃. *Polyhedron* **1**, 479-482 (1982).